Assessment of Laser Solid Freeform Fabrication for Realization of Shape Memory Alloy Components with Complex Geometry

by

Munther Abdullah Alhammad

A thesis
presented to the University of Waterloo
in fulfillment of the
thesis requirement for the degree of
Master of Applied Science
in
Mechanical Engineering

Waterloo, Ontario, Canada, 2008

Author's Declaration for Electronic Submission of a Thesis

I hereby declare that I am the sole author of this thesis. This is a true copy of the thesis, including any required final revisions, as accepted by my examiners.

I understand that my thesis may be made electronically available to the public.

Munther A. Alhammad

Abstract

The purpose of the present study was to assess the feasibility of a laser layer manufacturing technique for realization of shape memory alloy (SMA) components with complex geometry. Pre-placed laser solid freeform fabrication (LSFF) was utilized to produce straight and curvaceous SMA parts from a mixture of 55.2 wt%Ni - 44.8 wt%Ti powder. A pulsed Nd:YAG laser was used; while laser pulse width and frequency were held constant at what are considered their optimal values (4 ms and 50 Hz, respectively), laser energy and scanning speeds were varied across samples to determine appropriate values for fabrication of high quality SMA parts . Different pre-placed powder thicknesses were deposited and then mechanically and physically studied.

Optical microscopy, SEM, EDS, and XRD methods, as well as microhardness measurements, were used to examine the microstructural characteristics and hardness of the SMA samples. Also, differential scanning calorimetry (DSC) was performed to determine the transformation temperatures of the fabricated parts. The results confirmed the formation of crack-free solid surfaces in which two types of microstructure exist: solid (non-prose) and dendrite arms. EDS chemical composition analysis confirmed the absence of any impurity or oxidise in the cross section of the samples as well as the presence of only nickel and titanium. XRD spectrum analysis indicated the presence of Ni-Ti intermetallic phases, which are almost Ni-Ti but contain a small amount of Ti_2Ni. The XRD results also indicated the presence of austenite and martensite phases, which are exchanged during heating or mechanical deformation. The hardness of these samples varied from 250 to 450 $HV_{0.3}$.

Several tests were carried out to investigate the shape memory effect (SME). It was observed that the fabricated SMAs can recover from the bent condition very quickly (i.e., 1 to 8 seconds) depending on their thickness. In general, the fabricated parts were first bent out of their original shapes then heated, in various ways, above the transformation temperature.

To theoretically assess the SME performance of the fabricated SMAs with the proposed geometry two models were developed. The first model was established based upon a lump approach in which the part was exposed to an electrical current. The second model, however, was established based upon a finite element method in which a specific domain at one end of the sample was exposed to a source of heat. It was found that the theoretical outputs from both models were in good agreement with the experimental results.

Acknowledgements

I would like to take this opportunity to acknowledge the support of a number of individuals without whom this thesis would not have been possible. I would like to thank my supervisor, Dr. Ehsan Toyserkani for sharing his ideas with me, and helping me in all ways. As well, I wish to thank my examination committee, Dr. Hamid Jahed and Dr. Steve Corbin for their time and insight. I remain indebted to the Ministry of Higher Education in Saudi Arabia for giving me a once in my lifetime opportunity to go the added distance to complete this thesis.

It is a pleasure to thank the many people who made this thesis possible. Many individuals have contributed their time and expertise during different phases of this study. In particular, I would like to show my gratitude to Robert Wagner for all his knowledge and invaluable wisdom on machining; Dr. Yuquan Ding for SEM imaging; Dr. Li for his assistance on XRD analysis; and Dr. Paul for his technical assistance in performing LSFF techniques. They were always supportive and took time from their busy schedules to help me out.

I am indebted to my colleagues for providing a stimulating and fun environment in which to learn and grow. My colleagues have been of significant importance to me and they have provided an enjoyable social atmosphere in the lab. My ALFA and RPL friends, thank you all for your support and friendship. I would not be able to do this without you guys.

In closing, I would like to dedicate this thesis to my family who have supported me through more than two decades of my academic career. Their love and persistent support have always been my inspiration to achieve my goals. Lastly, I could not complete this thesis without plentiful support and love from my wife, thank you!

Table of Contents

List of Figures

List of Tables

Nomenclature

ρ	Mass density of SMA wire [kg/m^3]
ξ	Martensite volume fraction [%]
V	volume of wire [m^3]
T_0	Ambient temperature [°C]
R	Electrical resistance of SMA wire [Ω].
I	Current through SMA wire [A].
h	Convection heat transfer coefficient
T_s^M	Martensite starting temperature [°C].
T_f^M	Martensite finishing temperature [°C].
T_s^A	Austenite starting temperature [°C].
T_f^A	Austenite finishing temperature [°C].
E_a	Elasticity of austenite [MPa].
E_m	Elasticity of fully twinned martensite [MPa].
E_d	Elasticity of detwinned martensite [MPa].
E_T	Elasticity of partly twinned martensite [MPa].
c	Specific heat of SMA wire [J/(kg.°C)].
ε	Total strain.
σ	Total Stress [MPa].
C_m	Reciprocal of stress rate

Chapter 1

Introduction

The exciting field of smart materials, such as shape memory alloys (SMAs), is expanding rapidly in the direction of medical and robotic applications. In fact, smart biomedical materials already play a major role in replacing and improving the function of several body parts; for example, some common implants include hip joint replacements, artificial heart valves, dental implants and contact lenses. The primary advantages of utilizing SMAs in robotic applications are their small size, volume, and weight, high force to weight ratio, low cost and human-like behavior. They are currently being used in robotics actuators and micromanipulators to simulate human muscle motion.

Shape memory alloys are very attractive materials to a wide variety of sectors namely due to the fact that they demonstrate pseudo-elasticity and the shape memory effect (SME), which ordinary metals and alloys are incapable of. That is, a SMA is capable of recovering its original shape after large deformation if it is heated above its characteristic transition temperature or by releasing applied loads.

It was only relatively recently, in the early 1960s, that the shape memory effect in an alloy of nickel and titanium (Ni-Ti) was discovered. Since that time however, intensive metallurgical investigations have been made to explore the mechanics of its basic behavior. The use of Ni-Ti for medical purposes was first reported in the early 1970s. In the early 1980s, the idea gained more support and some orthodontic and experimental orthopaedic applications were released. It was only in the mid-1990s, however, that the

first widespread commercial Stent applications made their breakthrough in medicine. Currently, Ni-Ti seems to arouse notable interest in both the medical and commercial sectors.

When applied to certain surgical implants, Ni-Ti is expected to provide completely new functional capabilities, improved performance and the possibility of using minimally invasive techniques. It makes possible the fabrication of self-locking, self-expanding and self-compressing implants that are activated at body temperature. Within the last few years, several attempts have been made to use the advantageous properties of SMAs in robotics, micro-fluidic as well as pneumatic applications.

1.1 Manufacturing of SMAs

In spite of the great advantages associated with Ni-Ti, the manufacture of this material is still expensive and complex. The certified method of fabrication includes vacuum melting, hot and cold working, forming, heat treatment and machining. Also, compact sintering is used to fabricate SMA parts. Not only does this method use pure metal elements, but it involves complex processes from early preparation through to fabrication of the materials, requires special manufacturing facilities, such as high vacuum chambers, and takes an exorbitant amount of time to complete. In addition, most of the parts produced by this method are two dimensional simple shapes such as rods and sheets. There is an obvious need for a technology that can realize the fabrication of complexly shaped SMAs rapidly and reliably.

1.2 Objectives of the Thesis

The purpose of the work discussed in this thesis was to utilize the pre-placed laser solid freeform fabrication (LSFF) method to deposit a compound of titanium and nickel on mild steel and examine the possibility of forming SMA fabricated samples with complex shapes. Optical microscopy, scanning electron microscopy (SEM), energy dispersive spectroscopy (EDS) and X-ray diffraction (XRD) methods were used to examine the microstructural characteristics of the layers in cross-section. The evolution of the hardness of the samples as a result of surface modification caused by varying certain process parameters during fabrication was also evaluated. Two modeling approaches were used to gain insight into the performance of the fabricated shape memory alloy.

1.3 Outline

The present thesis is organized in the following order: In Chapter 2, background information on shape memory alloy physics and properties is provided, followed by descriptions of several SMA applications currently used in the medical and industrial sectors. Also provided in Chapter 2 is a discussion of typically used SMA manufacturing methods and an introduction to the laser solid freeform fabrication technique. Chapter 3 describes the material preparation, methodology, and experimental results of producing two types of SMA samples. This chapter also includes an investigation into the SME of the fabricated samples. In Chapter 4, two theoretical models for evaluating the performance of the samples are described. The first approach uses MATLAB to simulate the passing current model to estimate the total strain for four different curvaceous wires. Both COMSOL and MATLAB are applied in the second approach to simulate the one end heating model. Lastly, Chapter 5 offers conclusions as well as recommendations for future work.

Chapter 2

Literature Review

This chapter provides background information on shape memory alloy (SMA) physics and properties, as well as several descriptions of current medical and industrial applications of SMAs. Furthermore, this chapter contains considerable discussion of typical SMA manufacturing techniques with specific focus on the laser solid freeform fabrication (LSFF) method as a plausible improvement over the other methods.

2.1 Shape Memory Alloys: Physics and Properties

Shape memory alloys are very attractive materials which can regain their predetermined shapes if heated properly. This unique ability to return to the original shape after large inelastic strain (up to 10%) is known as the Shape Memory Effect (SME). This behaviour was first discovered in an Au-Cd alloy (1951), and then in a In-Tl alloy (1953) [1].

At low temperature phase (martensite), the material has the ability to be deformed easily, whereas at high temperature phase (austenite), the material tends to be brittle. By heating the SMA, the material regains its original shape by transforming from martensite to austenite as shown in Figure 2-1 and 2.2. This phenomenon is called "Martensitic Transformation", which can be defined as an atomic movement that causes a change in the lattice structure of the material, including sharing deformation [2]. The martensitic phase transformation can also be induced by pure mechanical loading while the material is in the austenitic phase, in which case detwinned martensite is directly produced from

austenite by the applied stress at high temperatures. There is another type of SMA which has a unique property called the two-way shape memory effect. In these SMAs, the materials have a unique shape for each phase (see Figure 2-3).

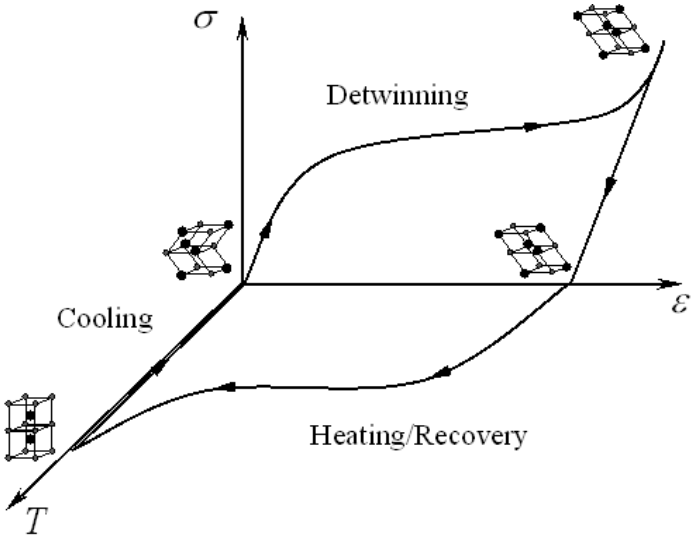

Figure 2-1: Stress-Strain-Temperature relation of SMA materials [3]

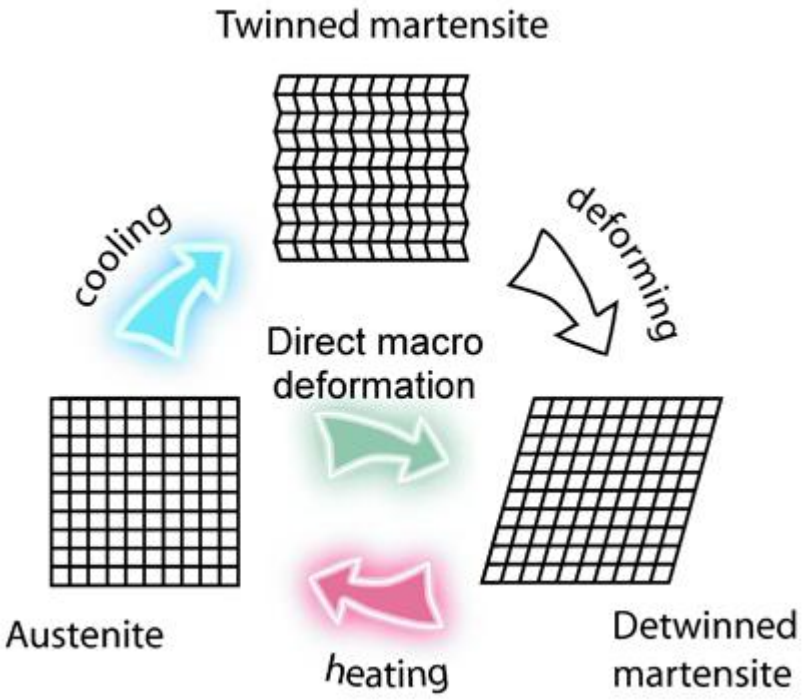

Figure 2-2: Phase transformation in SMAs [4]

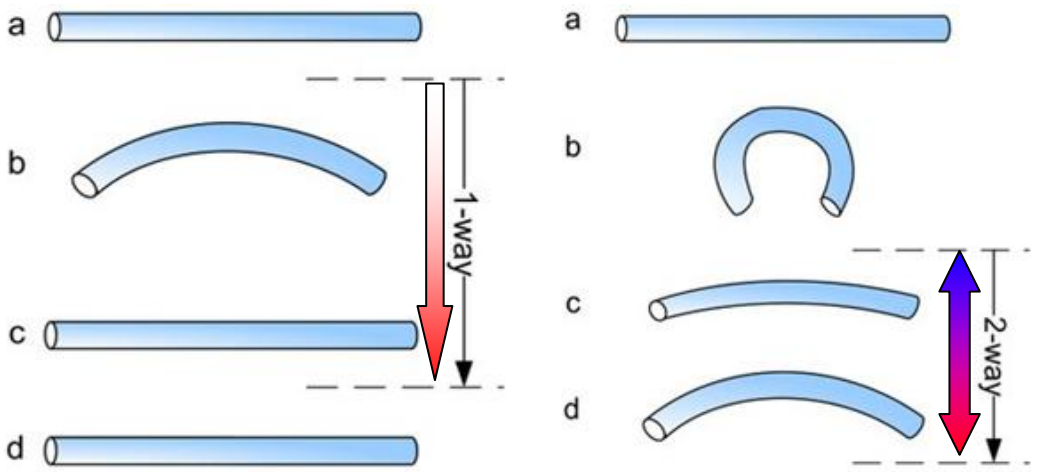

Figure 2-3: One-way vs Two-way SME [5]

Transformation occurs when the phase changes from one lattice structure to another, during heating or cooling. The phase transition temperatures, which, in simple systems, are identified as Ms, Mf (start and finish of the formation of martensite on cooling) and As, Af (start and finish of the formation of austenite on heating), strongly depend on the composition proportion of the materials used (see Figure 2-4). The austenite phase has a body center cubic (BCC) structure while the martensite phase has a monoclinic structure as shown in Figure 2-5. In addition to these two phases there is one more intermediate phase known as the R-phase which has the rhombohedral crystal structure, appearing in some special cases. In such cases, the direct transformation is a two-stage process, the material at high temperature in the parent phase (A) transforms to the intermediate phase (R) and then to the low temperature or product phase (M).

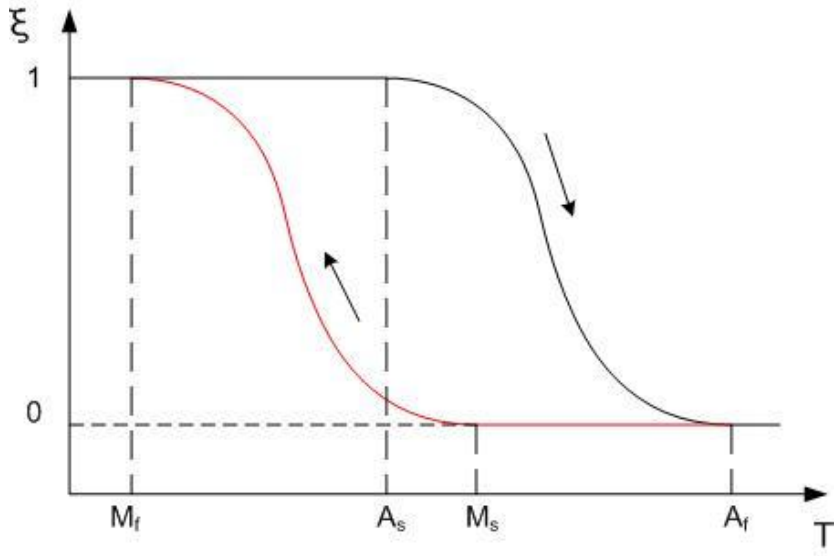

Figure 2-4: Phase transformation temperatures of SMA material [5]

Where ξ is the martensite fraction.

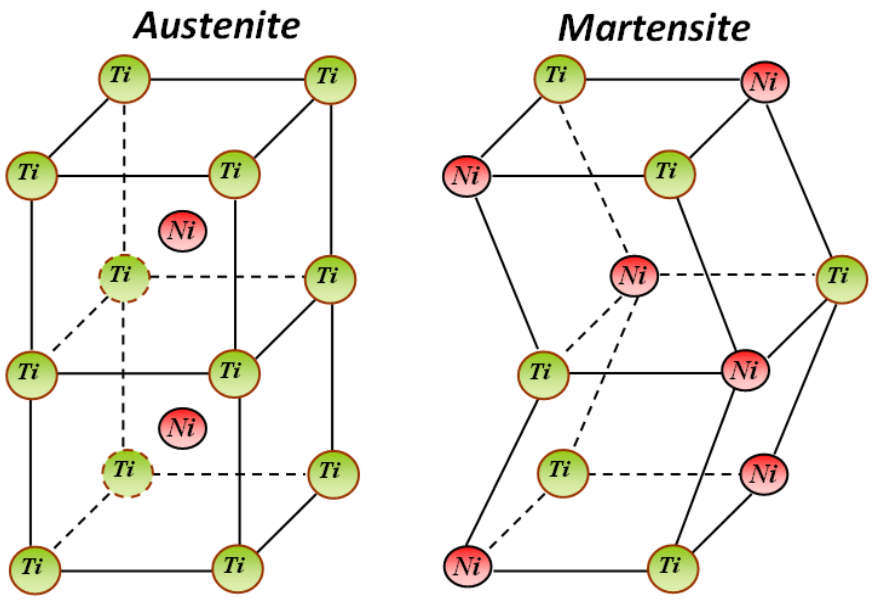

Figure 2-5: Lattice structure of the austenite and martensite phases

Among the many shape memory alloys listed in Table 2-1, Ni-Ti (NITINOL, 1960s) has the largest application potential because of its long fatigue life, large nonlinear elasticity and good corrosion resistance [6-9]. Other SMAs are not utilized in industrial

applications either because they are too expensive to fabricate or they can only be used in the form of single crystals [2]. Over the last three decades, the applications of the Ni-Ti alloy have increased in various fields including defense, medicine, manufacturing, and robotics. Therefore, unless otherwise specified the specific SMA studied in this work is NITINOL. The fabrication of these alloys is still expensive [5] mainly because of the fast reaction between the molten Ti and the oxygen [10][11].

Table 2-1: Shape Memory Alloys [12]

Alloy	Composition	Range of Tran. Temperatures (A_s) °C	Transformation Hysteresis °C
AgCd	*44~49 at % Cd*	*-190 ~ 50*	*~ 15*
AuCd	*46.5~50 at % Cd*	*30 ~ 100*	*~ 15*
CuAlNi	*14~14.5 wt % Al* *3~4.5 wt % Ni*	*-140 ~ 100*	*~ 35*
CuSn	*~15 at % X*	*-120 ~ 30*	
CuZn	*38.5~41.5 wt % Zn*	*-180 ~ 10*	*~ 10*
CuZn X ***(X = Si, Sn, Al)***	*Small wt % X*	*-180 ~ 200*	*~ 10*
InTl	*18~23 at % Tl*	*60 ~ 100*	*~ 4*
NiAl	*36~38 at % Al*	*-180 ~ 100*	*~ 10*
NiTi	*50 at % Ti*	*-50 ~ 110*	*~ 30*
TiNi X ***(X = Pd, Pt)***	*5~50 at % X*	*-200 ~ 700*	*~ 100*
TiNiCu	*~15 at % Cu*	*-150 ~ 100*	*~ 50*
TiNiNb	*~15 at % Nb*	*-200 ~ 50*	*~ 125*
TiNiAu	*50 at % Ni+Au*	*20 ~ 610*	
TiPd X ***(X = Cr, Fe)***	*50 at % Pd+X* *~15 at % X*	*0 ~ 600*	*~ 50*
MnCu	*5~35 at % Cu*	*-250 ~ 180*	
FeMnSi	*32 wt % Mn, 6 wt % Si*	*-200 ~ 150*	*~ 25*
FePt	*~25 at % Pt*	*~ -130*	*~ 100*
FePd	*~30 at % Pd*	*~ 50*	*~ 4*
FeNi X ***(X = C, Co, Cr)***	*Small wt % X*		

2.2 Applications of Shape Memory Alloys

The idea to exploit Ni-Ti SMAs in medical applications was first developed in 1978 by the Department of Bio-medical and Dental Materials Science in Shanghai. Only a few years later (1981), Ni-Ti applications were extended to instruments and devices for clinical usage. Now, Ni-Ti sheets and rods serve several industrial functions. A number of interesting results obtained from utilizing Ni-Ti SMAs in both industrial and medical applications are described in this section.

2.2.1 Industrial Applications

Pipe Coupling

Shape memory alloy pipe couplings have been used for several years. In this product, the SMA coupling is fabricated to have an inner diameter 4% smaller than the outer diameter of the pipe. When the couplings are cooled below their transformation temperatures (e.g. -20 ºC) using liquid nitrogen the inner diameter expands by approximately 7 - 8% [2]. Then, when the ends of two pipes are inserted into the coupling, the coupling is left to warm up until it reaches room temperature. Once heated, the coupling returns to its original diameter, and the ends of the pipes are bound together. A schematic diagram of how the coupling mechanism works is shown in Figure 2-6 [13].

SMA couplings have been installed in the hydraulic systems of F-14 jet fighters for several years now with no failures reported to date. There are two main advantages of using SMA couplings: (1) there is no welding required, so the surrounding materials will be saved from any damage that might occur from high temperatures, (2) maintenance is uncomplicated since the couplings can be removed easily by freezing them.

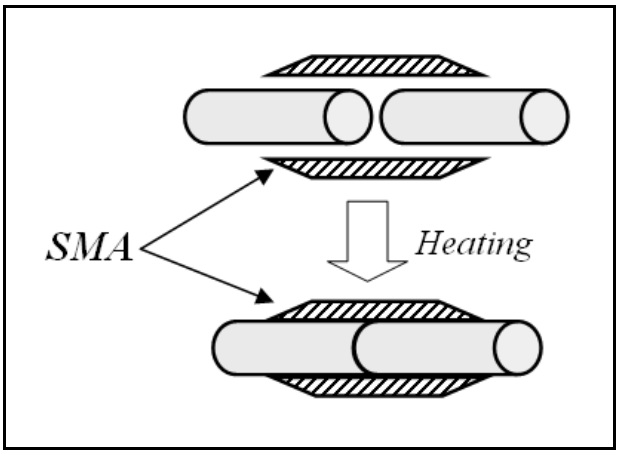

Figure 2-6: Shape memory alloy pipe coupling [13]

Actuators

Shape memory alloys have been widely used as actuators. Since SMAs are applicable for use as both temperature sensors and actuators, they have been very attractive in the robotics manufacturing sector. Typically, SMA actuators work using the two-way shape memory effect; their shapes can be changed back and forth by heating or cooling. The most common method used to heat these components is to apply electrical currents. However, other techniques have been used such as: blowing hot air, incident laser light, infrared rays, and currents of hot and cold water.

The two main advantages of SMA actuators are their small sizes and their ability to be installed in a wide variety of environments. Micro-manipulators with 6-mm long moveable parts are being successfully manufactured and tested (see Figure 2-7). A built-in SMA wire with 0.2 mm diameter and circular memorized shape is the main operator of this manipulator. The silicon rubber that covers the SMA wire acts as a bias spring that follows the wire's shape.

The second main advantage of SMA actuators is that temperature is the only environmental or atmospheric factor that affects the mechanical or microstructural properties of these alloys. Consequently, they can be installed in any condition without special adaptation, such as in a vacuum or under water. This characteristic makes it possible for SMA actuators to be installed in devices for positioning specimens in electron microscopes (Figure 2-8).

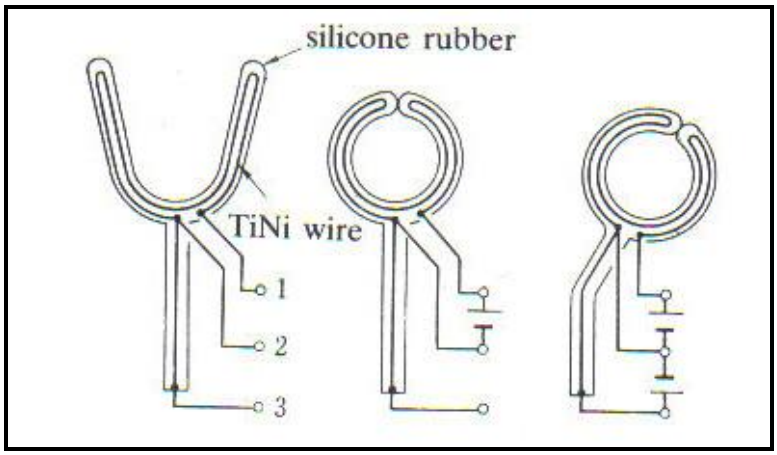

Figure 2-7: Construction of a shape memory alloy micro-manipulator [14]

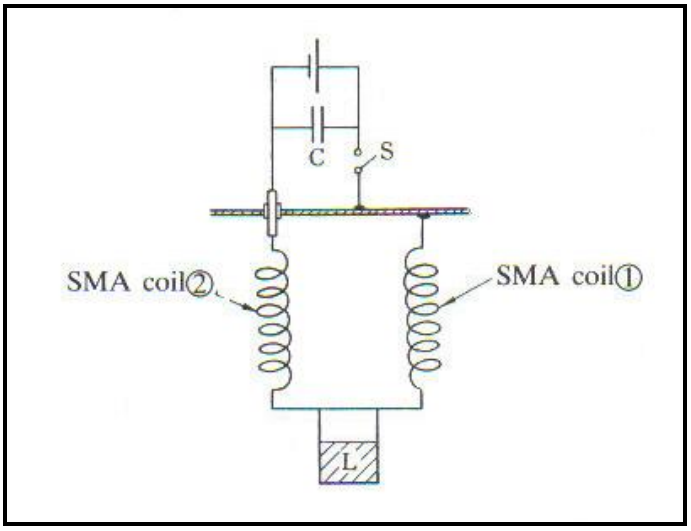

Figure 2-8: Device for positioning Electron microscope specimens [15]

2.2.2 Medical Applications

SMAs are one of the few materials currently used as prostheses or biomaterials in medicine and dentistry. The only other materials that have been sanctioned for implantation inside the body are: Fe-Cr-Ni, Co-Cr and Ti-Al-V. There are two unique properties that make these materials suitable for use inside the body: biofunctionability and biocompatibility. Biofunctionability can be defined as the ability of the material to perform the required function for the period it is expected to be in the body.

Biocompatibility refers to the ability of the materials to be nontoxic during the implanted period. Among the SMAs listed in Table 2-1, Ni-Ti (NITINOL) has received the most attention with regard to research and development of medical and dental applications.

Many dental and biomedical applications of SMA alloys have been successfully employed. Following a brief description of the use of SMAs in dentistry, three primary biomedical applications will be discussed, including cardiovascular, orthopaedic and surgical applications.

Dental applications

In dentistry, the most successful applications of SMAs are: dental arch wire, dental implants and attachments for partial dentures (Figure 2-9). SMA dental arch wires have been used primarily because of their superelasticity; however, the other two applications (i.e. dental implants and attachments for partial dentures) use the shape memory effect, unique to SMAs, as their fundamental property.

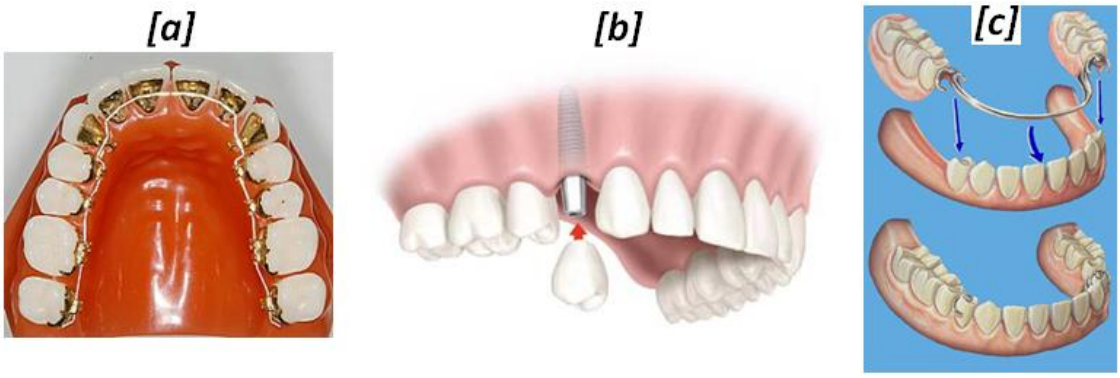

Figure 2-9: Dental application of SMAs a) dental arch wire, b) dental implants and c) attachments for partial dentures [16]

Sachdeva and Miyazaki [17] have reported that, using superelastic Ni-Ti arch wire produces faster teeth movement when compared with conventional stainless steel wire. This is because the superelastic behavior of the SMA provides a constant force and a large reversible deformation.

Cardiovascular applications

Figure 2-10 shows the first cardiovascular application developed with an SMA, the Simon filter [18]. This device was built to filter thickened blood from within the actual bloodstream, and is therefore especially applicable to persons who cannot take anticoagulant medication. The procedure of how this device works can be seen in Figure 2-11. Figure 2-11(5) shows the original shape of the filter before cooling, as well as the filter's final shape after deformation, insertion and re-formation within the bloodstream. That is, after fabrication the filter is first deformed and placed on a catheter tip as shown in Figure 2-11(1). In this shape and size the filter is easily inserted inside the bloodstream at a desired position, where it is released from the catheter tip. As the device is heated by the flow of blood it returns to its original shape, as illustrated in Figure 2-11(5).

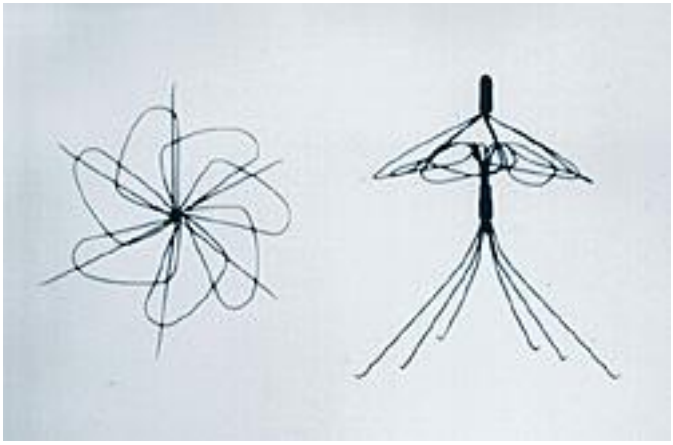

Figure 2-10: Cardiovascular application (Simon Filter) [19]

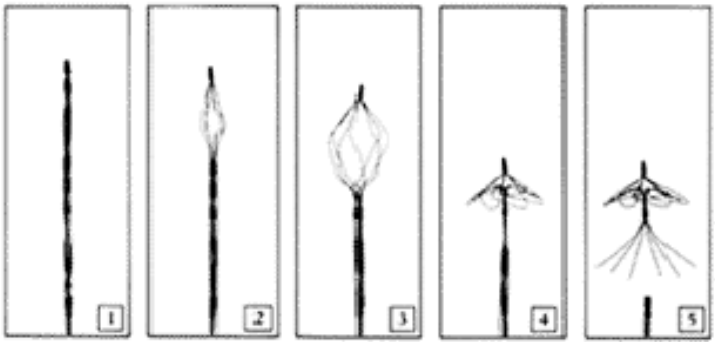

Figure 2-11: Steps of operation of Simon filter [20]

The second important SMA application in the area of cardiovascular medicine is the self-expanding Stent, named after the dentist C. T. Stent. The SMA stent is usually fabricated in the correct final size and shape, and then superelastically crushed into a diameter small enough to pass through a blood vessel on its way to its intended site, where it is released as shown in Figure 2-12. This kind of device has been found to be an ideal solution for many heart and/or blood problems, such as trouble passing fluid through the esophagus and bile duct [19], and blood vessels, such as the coronary, iliac, carotid, aorta and femoral arteries [21].

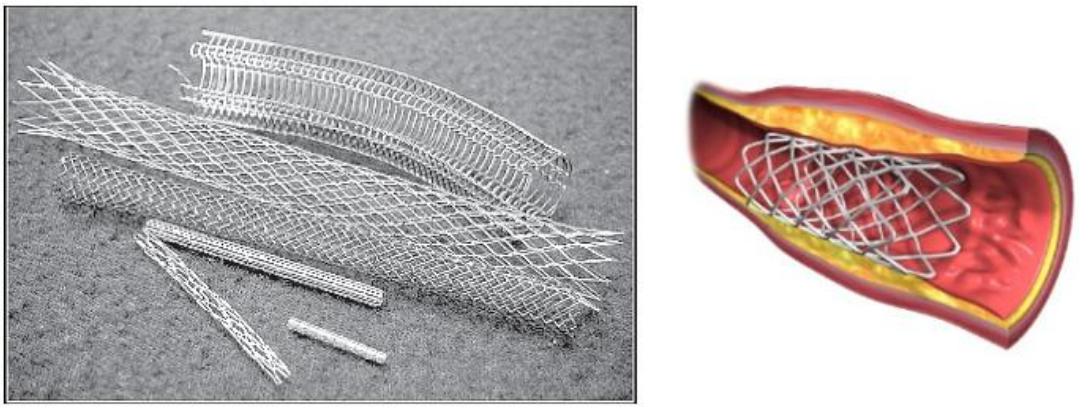

Figure 2-12: Self-expanding Stents [22]

Orthopaedic applications

SMAs have a large number of applications in the orthopaedic field. Bone plates are one of the orthopaedic applications used to assist in the healing of broken and fractured bones. Many types and shapes of SMA plates are used nowadays to stimulate the healing process; however, all of them have the same principle. The breaks are first set and then held in place using bone plates in locations where casts cannot be applied to the injured area. Because of the shape memory effect, after heating, these plates recover their former shape, exerting a constant force that tends to join parts separated by fractures, helping with the healing process [23]. Figure 2-13 illustrates this device [24]. Bone plates are often applied to fractures occurring to facial areas such as the nose, jaw or eye sockets.

Figure 2-13: Orthopaedic SMA device [24]

Surgical Instruments

Since medical researchers have made recent attempts to develop less invasive surgeries, shape memory alloys have been used to fabricate some surgical instruments. The two unique characteristics these materials have, superelasticity and the shape memory effect, are the main advantages of these tools.

Figure 2-14 shows an instrument used for endoscopic removal of kidney, bladder and bile duct stones and foreign bodies. This instrument, called a SMA basket, is inserted into the human body the same way Simon filters and self-expanding Stents are.. That is, the basket is cooled and supelastically compressed into a small enough shape for easy insertion into the body, as in Figure 2-14-a. After insertion and heating, the basket returns to its larger, final shape, as in Figure 2-14-b.

The use of SMAs to fabricate laparoscopic surgical instruments has also been successful. . Figure 2-15 shows some SMA surgical tools, such as grippers, scissors, and tongs. The ability to access complex places and maintain smooth movements are two important features this kind of tools should have.

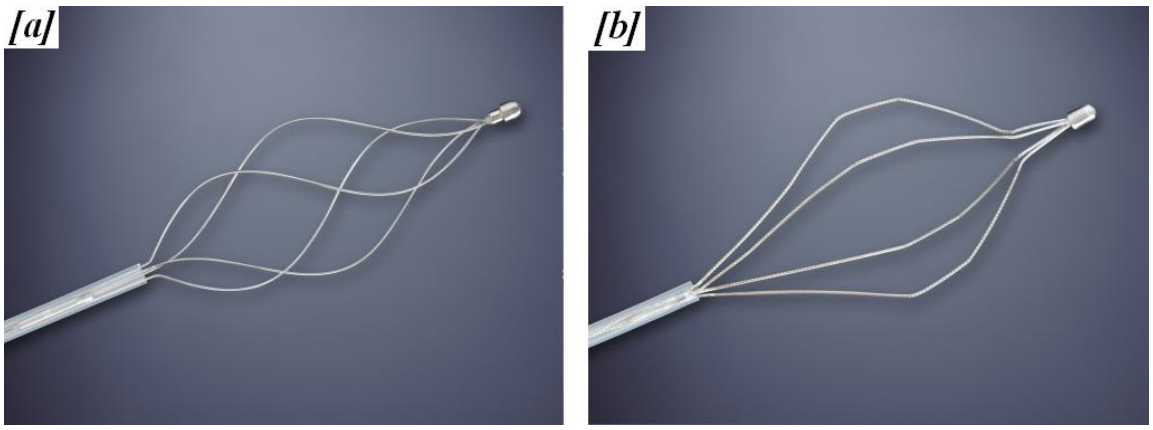

Figure 2-14: SMA basket a) deformed b) after heating [25]

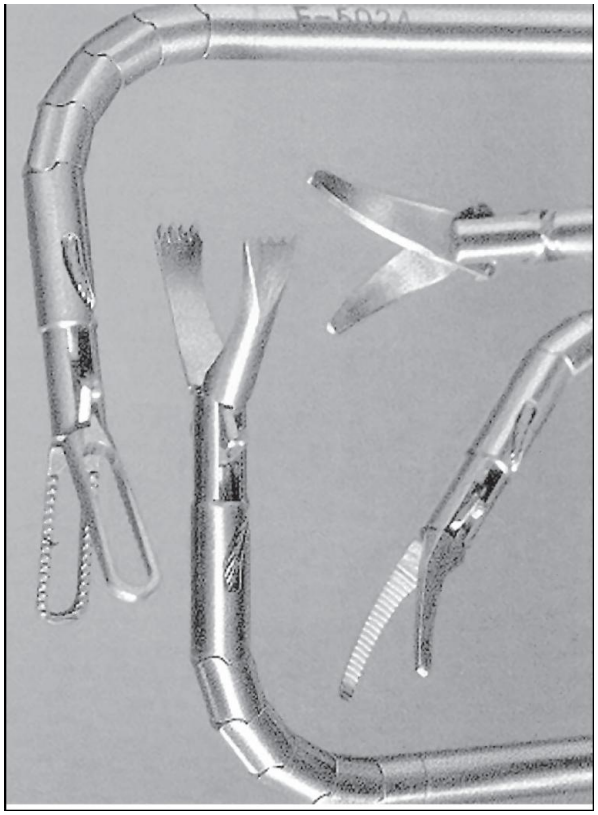

Figure 2-15: Laparoscopy tools (grippers, scissors, tongs and other mechanisms) [21]

2.3 SMA Manufacturing Techniques

At present, popular manufacturing techniques for production of the Ni-Ti alloy involve vacuum melting followed by hot and cold working [8,9,10]. As previously mentioned, phase transition temperatures strongly depend on the composition proportion of materials used. As low as one weight percent variation in Ni or Ti, shifts the transformation temperatures by 100 ˚C in the alloys with 55 wt% Ni or more [26]. This sensitivity to the chemical composition makes the manufacturing process difficult to control and ultimately arrive at desired SMA properties, particularly transformation temperatures. Shape memory treatment (heat treatment), forming and machining are additional steps needed to finalize the fabrication process of SMAs (see Figure 2-16). These necessary post-secondary treatments not only increase production cost and time, but also increase the complexity of the whole process. Meanwhile these techniques are not able to produce three-dimensional and complex parts.

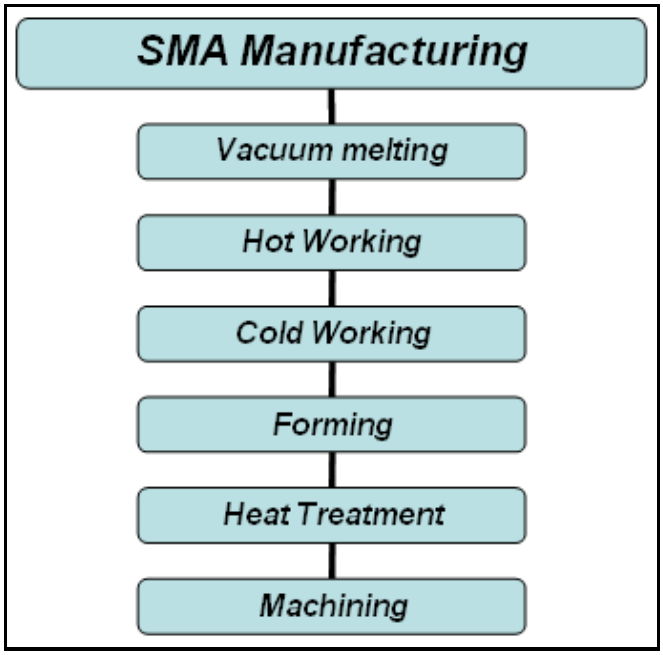

Figure 2-16: Fabrication process of shape memory alloy

2.3.1 Vacuum Melting

The most common method used to fabricate SMA parts is vacuum melting. Vacuum induction melting (VIM) and vacuum consumable arc melting (VAM) are counted among the most ideal production processes for SMAs [27]. Non-consumable arc melting, electron beam melting and plasma melting have also been assessed for production of SMAs; however, they are not very popular. Most manufacturers prefer using VIM due to the homogeneity of the chemical composition throughout the ingot and the controllability of the chemical composition during processing. Figure 2-17 and 2-18 show the appearance of the furnace and a schematic diagram of the operating system, respectively.

The crucible material (Figure 2-18) is usually graphite or calcia (CaO) because they allow for negligible oxygen contamination compared with aluminum or magnesia. However, the use of graphite may increase the carbon percentage in the molten alloy. By keeping the temperature inside the graphite crucible below 1450 ºC, the carbon level can be controlled between 200 and 500 ppm [28]. Shape memory alloy characteristics would not be affected by such a low amount. The other advantage of VIM is the high level of control permitted over the chemical composition (i.e., Ni-Ti percentage). The transformation temperatures can also be controlled within ± 5 ºC if the operation is carefully conducted [29]. For a smaller deviation, an in-situ composition control process is needed where the samples are taken from the molten metal and the transformation temperatures are quickly analyzed for immediate modification.

Figure 2-17: Front view of a vacuum control furnace [30]

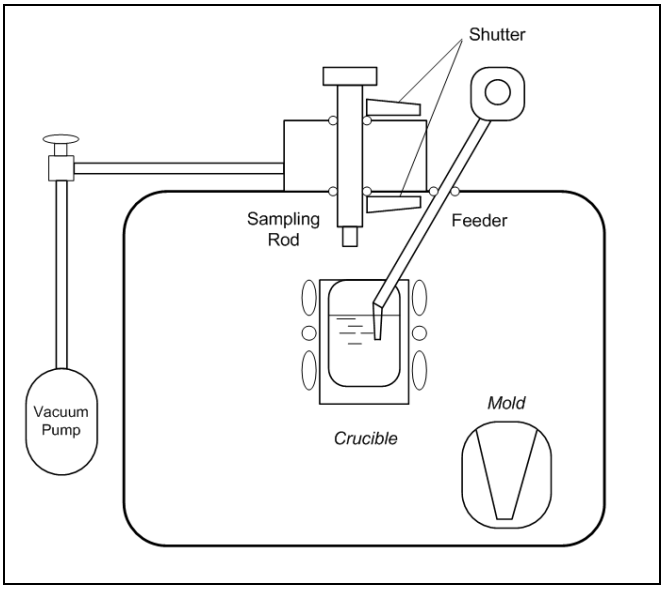

Figure 2-18: Operation system of in-situ composition control furnace

2.3.2 Hot and Cold Working

After melting and removing the surface layer, cold and hot working processes are applied to reach the desired dimensions. To control the oxidation, the highest temperature NITINOL can be hot worked at is 800 °C [28]. NITINOL billets and tubes have been tested using extrusion [31]. Other factors that might be affected by high temperature hot working are elongation and tensile strength, as shown in Figure 2-19. At 300 °C, the tensile strength begins to decrease, and at 500 °C, elongation starts to increase significantly until it reaches 120 % at 850 °C.

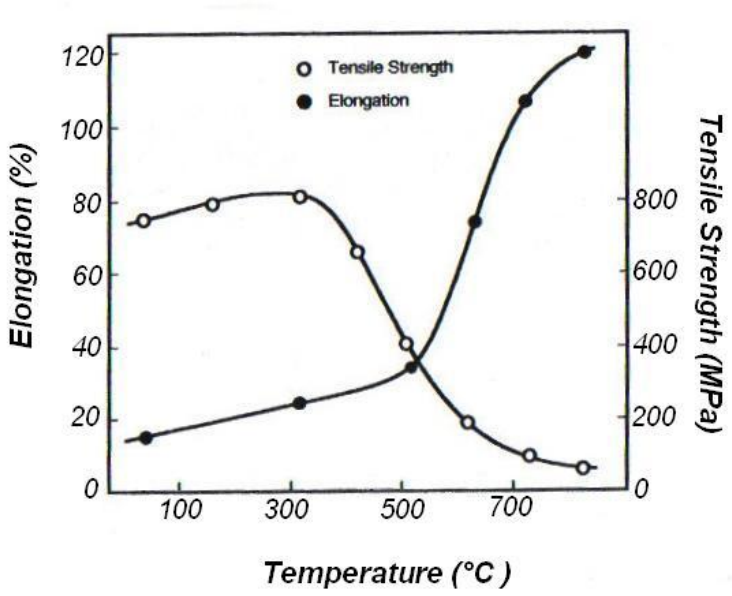

Figure 2-19: Tensile strength and elongation of a 50% Ni -Ti alloy

A number of difficulties can occur during the cold working process because of rapid work-hardening. As with any SMA, chemical composition plays a significant role in the workability strength of the Ni-Ti alloy; it becomes harder with increasing Ni contents. To reach the final dimensions, the NITINOL part should pass through several reduction stages with annealing at 600-800 °C. When the annealed NITINOL wire is deformed, tensile strength reaches 1000 MPa at 40 % strain.

Die drawing processes are being used to produce small size round wires while flat rectangular wires can be manufactured using cold rolling. Lubrication of these processes have been done to reduce the work temperature and the adhesion to the tools using sodium stearate soap [32], molybdenum disulfide [33], graphite-containing water based lubricant [34] and oil based lubricant [35]. Cold working has also been used to manufacture NITINOL tubes with minimum outside diameter sizes of 0.25mm [36]. Until now, shapes and sizes produced by hot and cold working processes have been limited.

2.3.3 Forming

Most cold-drawing SMA wires are finally shaped by forming. Forming SMA parts is difficult at ambient temperature due to their superelasticity features. Because of the large spring-back effect of SMAs, they need large forming amplitudes to produce the intended shapes. Figure 2-20 shows one of the efficient machines that can be used to form SMA parts. The forming process may be complex depending on the nature of the application and the parts may therefore have to go through a multi-stage process to attain their final shapes, see Figure 2-21.

Figure 2-20: Front view of an automatic forming machine [37]

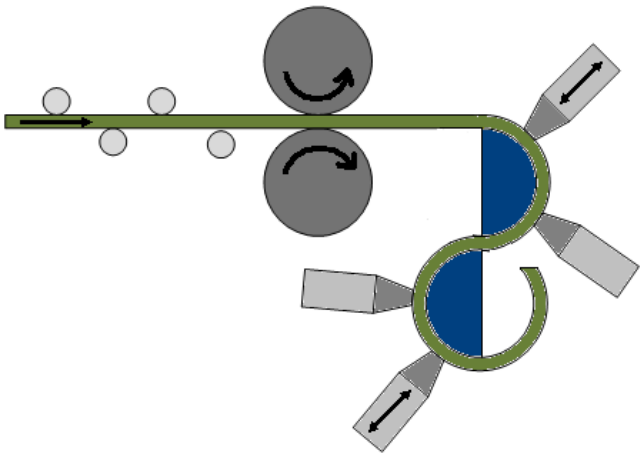

Figure 2-21: Operation principle of the forming machine

2.3.4 Heat Treatment

SMA parts are usually heat treated to obtain desired physical and mechanical properties. A range of 350-450 °C has been found to be a suitable heat-treating range for NITINOL materials; it is also called "Medium Temperature Treatment" [38]. The formed NITINOL parts need to be fastened on a jig during heating to ensure that their shapes do not change. Depending on the part size; the treatment time varies from 10 to 100 minutes. For alloys with 55.5 wt% Ni or more, higher temperatures are needed (600 – 900 °C) to achieve optimized properties [39].

In addition to the medium temperature treatment, a number of other methods of shape memory treatments have been used. Low temperature treatment is one of these methods. After forming the parts to the desired shape at room temperature, they are heated to 200 – 300 °C for 1 – 2 hours. Aging treatment is also applied as a heat treatment method for all-round (two-way shape memory alloy) parts [40]. A NITINOL part is first solution-treated at 800 °C at which point it is fixed as an arch shape. Then, the part is heated for 100 hours at 400 °C.

2.3.5 Machining

Although it is not important for SMA parts to be machined to improve their corrosion resistance, they can be machined using customary techniques such as: milling, turning and drilling. Tungsten carbide cutting tools have been found to be the best cutting tools due to their high tool life. On the other hand, strong alloys like NITINOL need more abrasive and modern processing, such as grinding, swing, water jet cutting and laser machining. In particular, laser cutting, using an Nd:YAG pulse laser, has become a preferred process for machining NITINOL. A CNC motion control system is capable of rapid prototyping with high speed and high accuracy.

2.4 Laser Solid Freeform Fabrication (LSFF)

Since the invention of the laser in the 1960s [41], applications for its use have increased exponentially in several areas, such as the automotive, navy, aerospace, and defence sectors, among many others. All of these applications have been adapted because a single laser machine is capable of performing the workload of several other 'ordinary' machines, such as welding, hardening and cutting machines. In addition, a new application of the laser has recently been invented by Steen (1988) [42][43], called laser solid freeform fabrication (LSFF) or, sometimes, Laser Cladding. The LSFF method has received a great deal of attention due to its expanded potential for material processing, such as metallic coating, high-value components repair, prototyping, and even low-volume manufacturing.

In the LSFF technique, the laser beam melts the desired alloy powder to create a thin layer on a moving substrate [44]. The technique can be used for rapid prototyping of complex shapes when the power is added to the process zone in a layer by layer fashion [45]. Depositing the materials on the substrate is performed using one of three methods: powder injection, pre-placing the powder on the substrate, or by wire feeding. LSFF with pre-placed powder technique is also called "selective laser sintering of metals" (SLSM) [46], or "direct metal laser sintering" [47].

A number of benefits can be expected from the use of the LSFF technique, since it overcomes the limitations of already existing metal fabrication techniques. These benefits are as follows:

1. Reduction of production time,
2. Enhancement of thermal control,
3. Parts repair,
4. Production of functional graded parts,
5. Production of smart structures.

Basically, there are two different techniques of LSFF: a one-step process and a two-step process. Figure 2-22 presents schematic representations of both techniques [48]. In Figure 2-22(a) the powder has been pre-placed prior to being melted with laser irradiation on a moving substrate. However, in Figure 2-22(b), an additive material is fed into the melt-pool. The additive material may be supplied in three different ways: paste, powder injection or wire feeding, as shown in Figure 2-22(b) (1), (2) and (3), respectively. Since the work described in this thesis only used the two-step fabrication process, it will be explained in some detail.

Two-step LSFF (Pre-placed)

The pre-placed laser solid freeform fabrication technique is a simple method which has been used successfully to coat and prototype several materials. Bonding and coherence between the powder and the substrate are important issues that must be taken into account in this technique. It is also important to prevent the powder from being sprayed due to the gas flow during the second stage. These issues can be overcome by using a chemical binder. The chemical binder helps the powder particles to adhere to the substrate during the process. However, any evaporation that occurs may increase the porosity percentage in the fabricated wire.

The second step of the process is to pass the laser beam over the pre-placed powder. This step creates some phenomena, such as: creation of a melt-pool on top of the surface, expansion of the melt-pool to the interface with the substrate, and penetration of heat to the substrate.

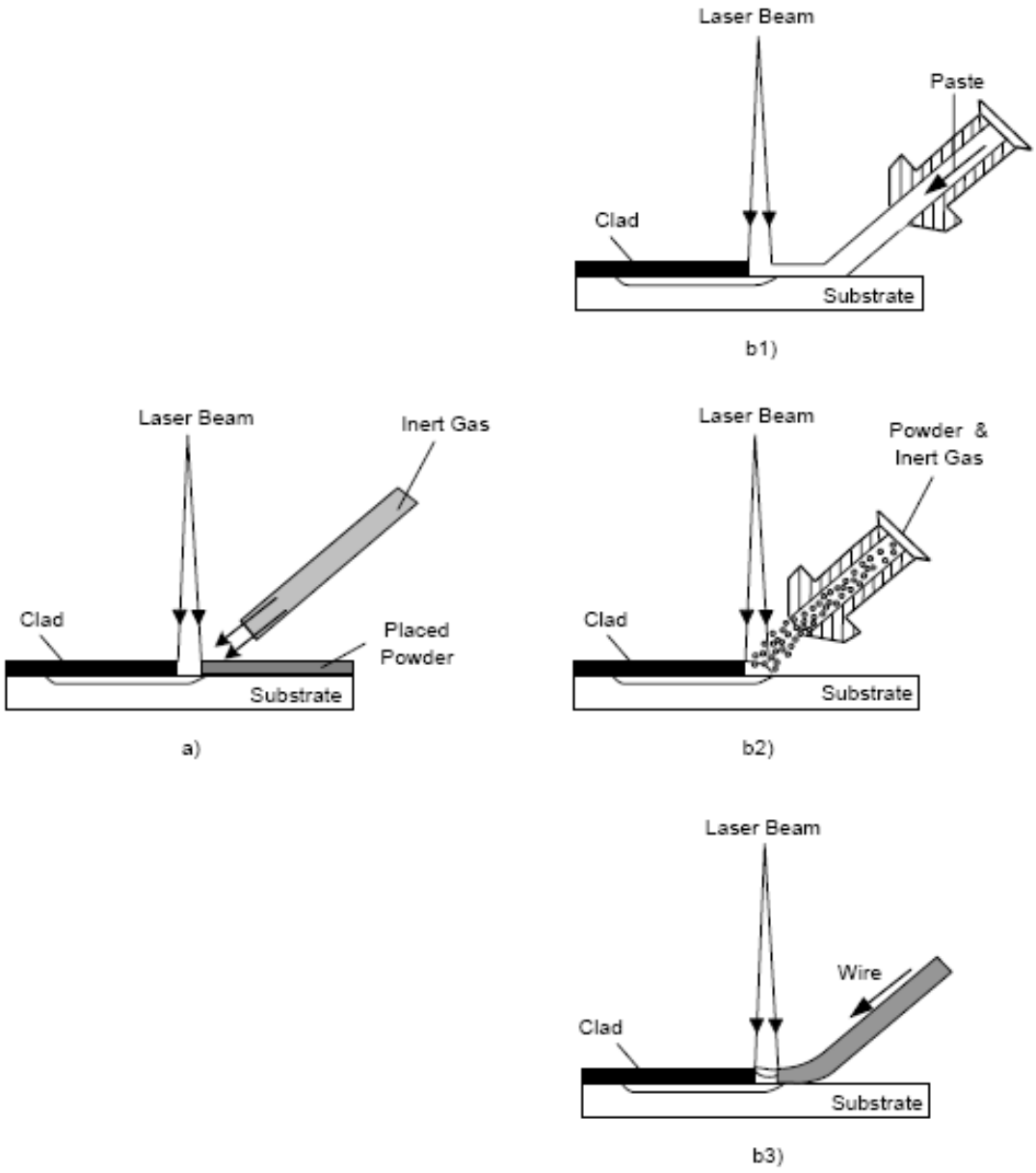

Figure 2-22: Different methods of LSFF: a) two-step LSFF, b) one-step LSFF, including b1: paste LSFF, b2: powder injection LSFF, b3: wire feeding LSFF [44]

Several laser material processing techniques have been considered for melting of titanium-nickel alloys. Laser Direct Metal Deposition (LDMD) has been used by Malukhin and Ehmann [49] to fabricate Ni-Ti round plates in a 25.4 mm diameter ingot. Malukhin et. al. used a Ti substrate to ease the debonding since Ni-Ti and Ti have different thermal expansion coefficients.

2.5 Modeling of Shape Memory Alloys

Shape memory alloy modeling has been expanded in the last two decades. Two groups of models have been developed to express SMA hysteretic behavior. The first group uses the classical theory of plasticity to predict SMA behavior, while the other uses the Preisach model, which was first developed in 1935 [50].

From 1982 until 1989, Tanaka [51] [52] used the martensite volume fraction as an internal equation to relate temperature and stress to predict the superelastic behaviours of SMAs. In 1990, Liang predicted a modified model using cosine low of the martensite fraction [53]. The martensite fraction was then used to involve the twinned and detwinned behaviour of the SMAs in a new model conducted by Brinson in 1993 [54]. Boyd and Lagoudas in 1994 [55] have developed a three dimensional model using Tanaka's model to predict a model with elastic and transformation properties of SMA materials. SMA modeling has received a great deal of attention over the last two decades; however, most of these simulation models have limited applications.

More models have been developed for expressing SMA hysteretic behaviour with careful thermodynamic considerations. Ivshin and Pence [56][57] have developed a powerful model for SMA behaviour simulation. Their model takes into consideration heat energy balance from heat exchange, latent heat and external heat sources.

In 2002, Shaw [58] developed a model that may be counted as the first completed model. The model is capable of simulating not only the superelasticity and the shape memory effect of SMAs, but also unstable phase transformation behaviours. In addition, it includes parts for heat balance, which makes it suitable for modeling actuators.

Another model that has recently been applied to SMA actuator applications was originally developed by Ikuta et al. [59]. Ikuta's mathematical model uses lumped parameters in a convective heat transfer equation to generate \temperature profiles for SMAs.

2.6 Summary

The great properties SMAs have and their abilities to be effective in several fields of application make it essential for these materials to be manufactured easily with different shapes and sizes. LSFF is a promising technique for manufacturing especially complex or small parts.

Chapter 3

Characterization of Pre-Placed LSFF for production of SMA Parts

The experimental work was divided into two steps; the first was to fabricate SMA parts using laser solid freeforming (LSFF) while the second was to investigate the mechanical and metallurgical characteristics of the formed parts. The pre-placed LSFF process was used to melt the Ni-Ti mixed powder in a controlled shield gas (Argon) atmosphere to produce a 30×1×1 mm SMA straight wire and a circular wire with diameter of 20 mm.

3.1 Manufacturing Technique

A pulsed Nd:YAG laser manufactured by LASAG with a maximum power of 1 kW was used in this study. The process parameters, such as laser pulse energy, laser pulse width (duration) and scanning speed, were optimized to effectively arrive at desired mechanical and physical properties as well as the required SME. The SMA samples produced by this technique were tested experimentally to determine their quality at different process parameters (see Table 3-1).

The laser beam energy distribution was Gaussian with TEM00 mode, and the beam spot diameter on the powder bed was 1.4 mm. A schematic representation of the pre-placed LSFF process is shown in. In order to melt the powder, the laser beam remains

stationary while the pre-placed powder substrate is moved in a rectilinear direction using a CNC machine stage. This process results in a melted layer of the alloy powder that has become bonded to the substrate.

Nearly pure (99.5%) Titanium and nickel powders from Alfa Aesar, with average mesh sizes of -325 (44 μm) and spherical shapes, were used in this experiment. These powders were combined, but were weighted to be wt%55.2 Ni and wt%44.8 Ti, and left mixed for approximately 24 hours. The powders were weighted in this way so the resulting alloy powder would contain the same weight percentage distribution as Ni-Ti (NITINOL), as shown in the Ni-Ti alloy system (Figure 3-2). In this study, a thin plate of mild steel with 0.65 mm thickness was used as a supporting substrate for placing the alloy powder. This thin plate was chosen to ease the debonding process and separation of the SMA from the substrate once produced. Two additional plates, each 2.2 mm thick, were used not only to support the thin plate, but also to ensure the exact thickness of the pre-placed powder. As Figure 3-1 (b) indicates the addition plates created a channel that the powder could be pasted into.

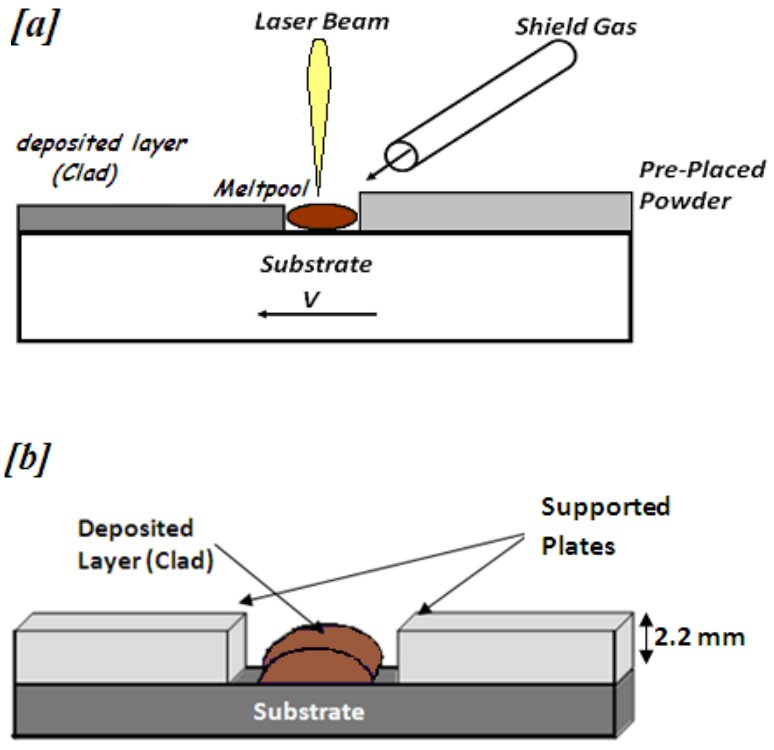

Figure 3-1: Schematic diagram of the pre-placed LSFF process

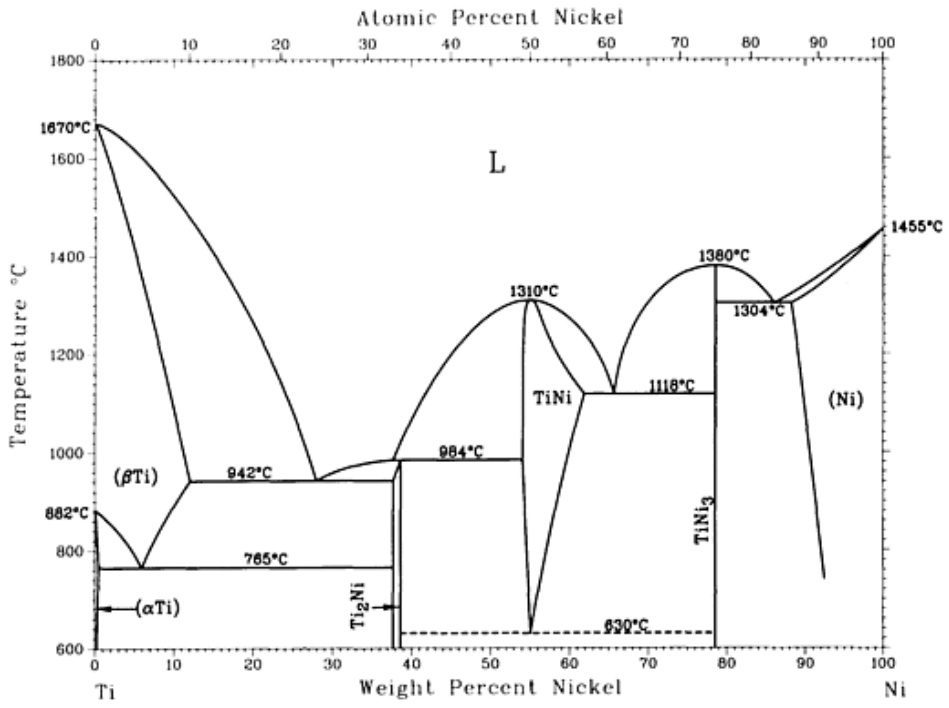

Figure 3-2: Ti-Ni phase diagram [50]

Using the above manufacturing technique, several samples were fabricated. Figure 3-3 shows a number of straight wires immediately after the LSFF process was completed (before debonding and grinding). By bending the thin steel plate (substrate), the samples started to separate by themselves, see the upper end of the samples in Figure 3-3. Figure 3-4 presents several prepared curvaceous samples with different shapes and sizes after grinding.

Figure 3-3: SMA Straight wires before debonding and grinding

Figure 3-4: Several prepared curvaceous samples with different shapes after grinding

3.1.1 Process parameters

Since several parameters do not contribute significantly to the quality of fabricated SMA parts, they are typically held at fixed values during processing. For example, in this study, the best values for the laser pulse width and the laser frequency parameters were found to be 4 ms and 50 Hz, respectively, and were therefore held constant. However, to fabricate straight wires, laser energy and scanning speeds were varied from 2 to 6 J and from 2 to 6 mm/s, respectively. In this range, fifteen samples were chosen to be studied, as listed in Table 3-1. These samples were divided into three groups: low energy input (samples S1-S4), moderate or standard energy input (S5-S11) and high energy input (S12-S15).

For fabrication of curvaceous samples, laser pulse width and laser frequency were again held constant at 4 ms and 50 Hz, respectively. However, laser scanning speed and laser energy were varied from 2 to 4 mm/s and from 2 to 6 J, respectively. As listed in Table 3-2, nine samples, equally distributed into low, medium and high energy groups, were produced using these parameters. The pre-placed powder thickness of the samples listed on Table 3-1 and Table 3-2 was fixed on 2.2 mm.

Table 3-1: Process parameters for fabrication of straight samples

Sample #	Laser Energy (J)	Pulse Width (ms)	Laser Frequency (Hz)	Scanning Speed (mm/s)
S1	2	4	50	6
S2	2	4	50	5
S3	2	4	50	4
S4	2	4	50	3
S5	2	4	50	2
S6	4	4	50	6
S7	4	4	50	5
S8	4	4	50	4
S9	4	4	50	3
S10	4	4	50	2
S11	6	4	50	6
S12	6	4	50	5
S13	6	4	50	4
S14	6	4	50	3
S15	6	4	50	2

Table 3-2: Process parameters for fabrication of curvaceous samples

Sample #	Laser Energy (J)	Pulse Width (ms)	Laser Frequency (Hz)	Scanning Speed (mm/s)
C1	2	4	50	4
C2	2	4	50	3
C3	2	4	50	2
C4	4	4	50	4
C5	4	4	50	3
C6	4	4	50	2
C7	6	4	50	4
C8	6	4	50	3
C9	6	4	50	2

3.2 Experimental Test Devices

3.2.1 Metallurgical Analyses

Several material characterisation tests were conducted to examine the properties of the produced SMAs. The metallurgical properties of the fabricated SMA sample cross sections, as well as the shape memory effect (SME) and elasticity of the produced samples were studied.

The cut samples were mounted in epoxy resin and then polished using standard polishing procedures for microscopy observations or hardness tests. The microscopy samples were then etched using a mixture of NHO_3 and HF (volume ratio: $2NHO_3$, 1HF, $17H_2O$) prior to testing. A BH2-UMA model Olympus microscope was used for optical microscopy. A Jeol: JSM-6460 Scanning Electron Microscope, equipped with Oxford Instruments' INCA X-ray chemical analysis instrument was used for SEM and energy dispersive spectroscopy (EDS) tests. X-ray diffraction (XRD) analyses, with Cu-K_α radiation, were conducted using a Rigaku: SA-HF3 X-Ray generator machine, which was operated under 50 kV voltage and a 40 mA current. The diameter of the XRD collimator was set to be square shaped, with 0.3 mm width, and the 2θ angles between 20° and 90° were scanned. Hardness measurements were made using a LECO: MHT Series 200 Vickers microhardness tester and 300g loads.

Several tests were carried out to investigate the shape memory effect (SME) of the formed samples. Transformation temperatures of the prepared samples were determined from 25°C to 120°C using NETZSCH (DSC404c) equipment at the same heating and cooling rate of 2K/s. The DSC was used to analyse the thermal nature of SMA samples to compare the results with those previously reported for formed samples fabricated with different process parameters.

3.2.2 Sample preparation

The rest of the samples (uncut) were delaminated from the substrate by bending the substrate. The separated samples were then grinded, not only to remove any oxidized and diluted layers generated by the intrusion of the tempo and supportive substrates, but also to achieve the final dimensional features. A manual grinding wheel was used to obtain the final dimensions of the straight wires (30×1×1 mm). In the case of the semi-circular wires, the process was more complex. To grind the inside face of the samples, a circular heat grinder was used. A jack was used to hold the samples while the inside face is grinded, see Figure 3-5.

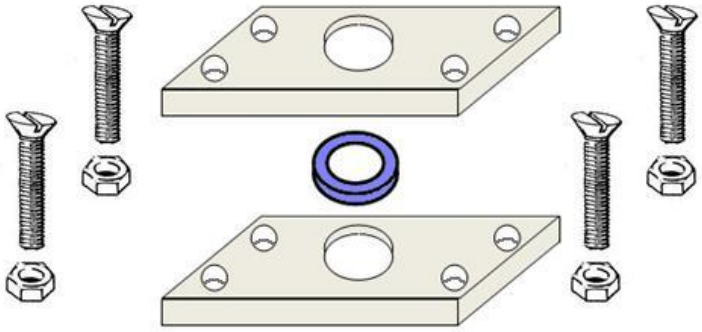

Figure 3-5: Schematic diagram for grinding process for the semi-circular samples

3.3 Results

In order to examine the SMA characteristics, several tests were conducted. Some of them were to study the metallurgical properties such as the type of microstructure by inspecting the part cross-section. However, the others were to study the mechanical properties such as hardness. The effect of the process parameters (i.e., scanning speed and laser energy) were studied in details in this section.

3.3.1 Optical Microscopy

Figure 3-6 depicts two straight sample cross-sections from SMA layers produced from different pre-placed powder thicknesses, while all other parameters were kept constant. The height of the layers for samples prepared with 2.2 and 1.0 mm pre-placed powder thicknesses were reduced to 1.5 and 0.8 mm, respectively, as seen in Figure 3-6 (a) and (b). The relationship between the thickness of the powder and the height of the straight sample is presented in Figure 3-7. The results of the trial experiments with the powder pre-placement thickness of 3 mm have shown that the formed layers are prone to severe cracking. Interestingly, initial powder thickness is not the only factor that affects layer height; results indicate an inverse relationship between laser scanning speed and deposited layer height, in that as scanning speeds increase layer height decreases.

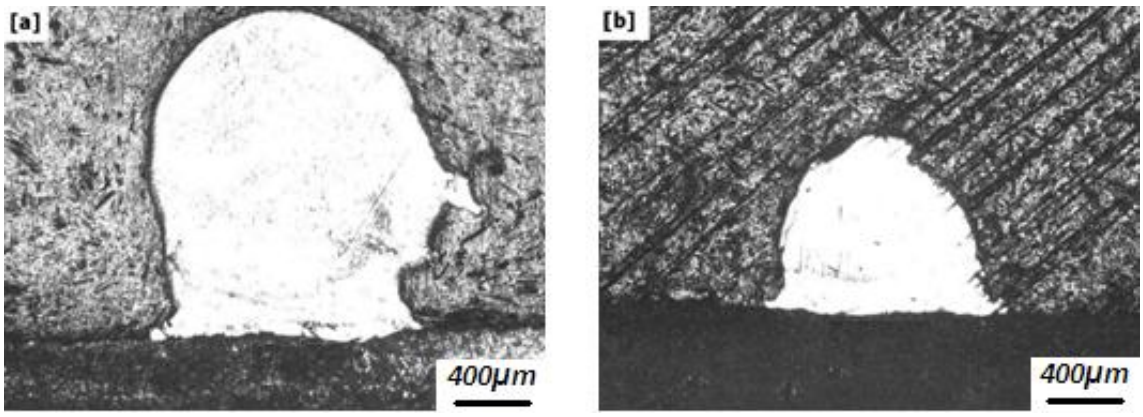

Figure 3-6: Optical Micrographs of cross sectional view with pre-placed powder thickness of (a) 2.2 (b) 1.0 mm

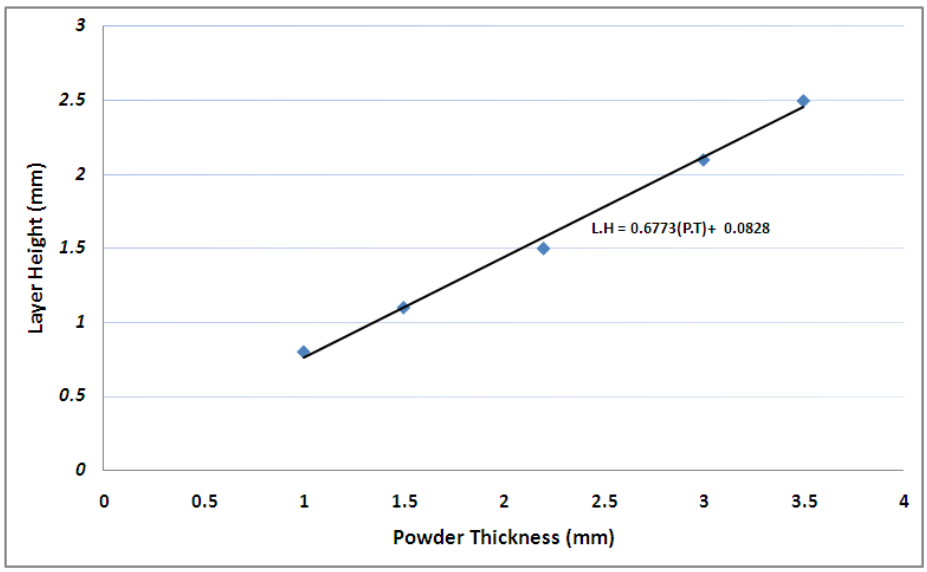

Figure 3-7: Powder thickness-Layer height Relationship

3.3.2 Scanning Electron Microscopy

The scanning electron microscope (SEM) was used to analyse the microstructure and the possible porosity percentages of the fabricated samples. An SEM image taken at the center of a cross-section of sample S8 processed with 4 mm/s laser scanning speed and 4 J laser energy, is shown in Figure 3-8. The result shows a crack-free, solid surface that includes two types of microstructure: solid and dendrite arms. In some samples, the SEM results indicate the presence of a small percentage of porosity, see Figure 3-8. A higher magnification image was taken of this porosity to identify the shape and size of the pores. Figure 3-9 shows that the pore structure contains two shapes: open and interconnected, and closed and separated from each other. The size of these pores varies from 1 to 10 µm in diameter.

The dendrite structure was also magnified using SEM. Figure 3-10 shows the dendritic structure formed in the middle of the sample cross section. The percentage of these dendrite arms are strongly related to the certain processing parameters, such as laser energy input and laser scanning speed. It is noted that dendrite arms spacing (DAS) decreases significantly with increasing laser scanning speeds. To illustrate, Figure 3-11

shows the dendrite arms in a cross-section of sample S10, which was processed with 2 mm/s scanning speed, where the dendrite arms are very wide, unlike sample S8. Interestingly, other results indicate that DAS can be eliminated totally by increasing the input energy. The results in samples S11-S15 showed no percentage of DAS in the cross section.

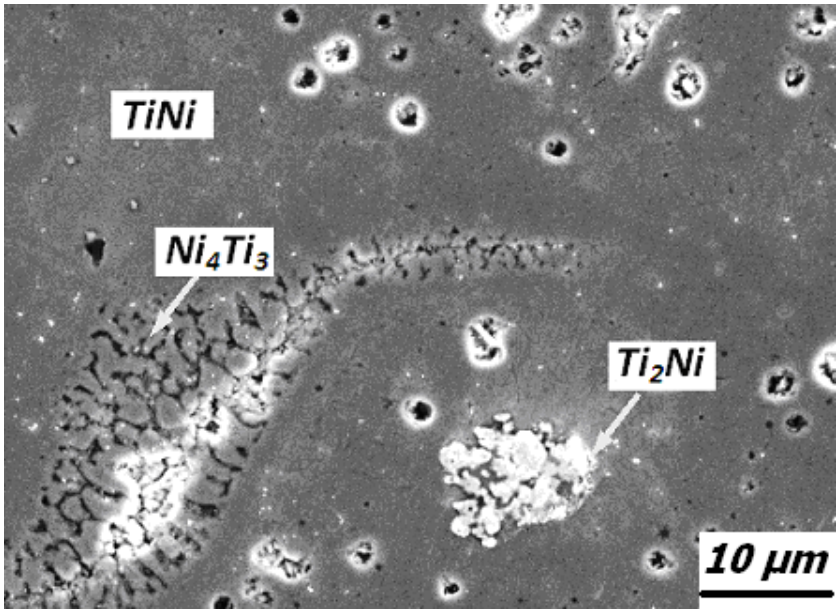

Figure 3-8: SEM micrograph of the sample S8 cross section

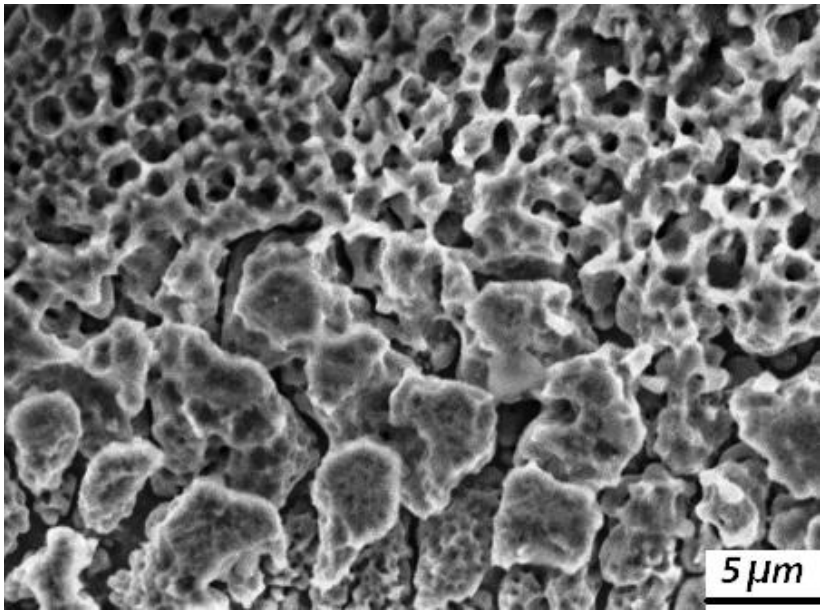

Figure 3-9: SEM micrograph of the porosity area

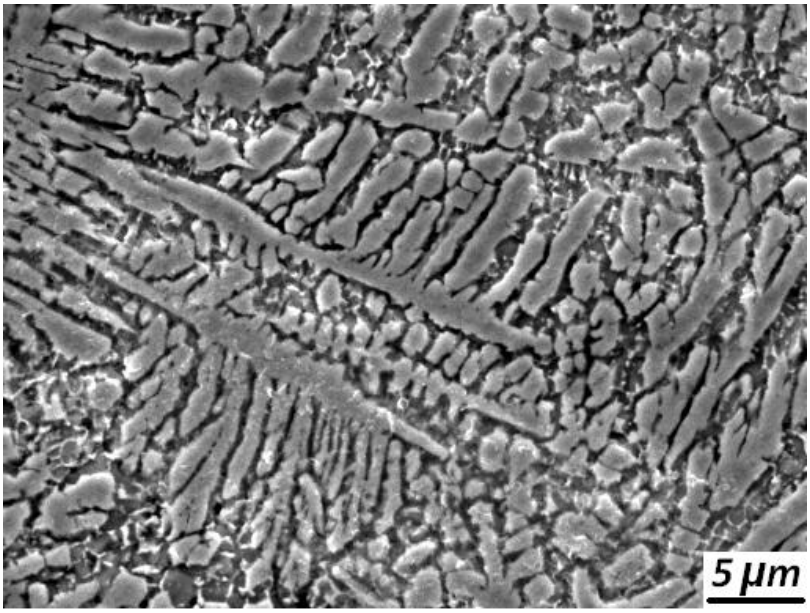

Figure 3-10: SEM micrograph of the dendrite arms in sample S8

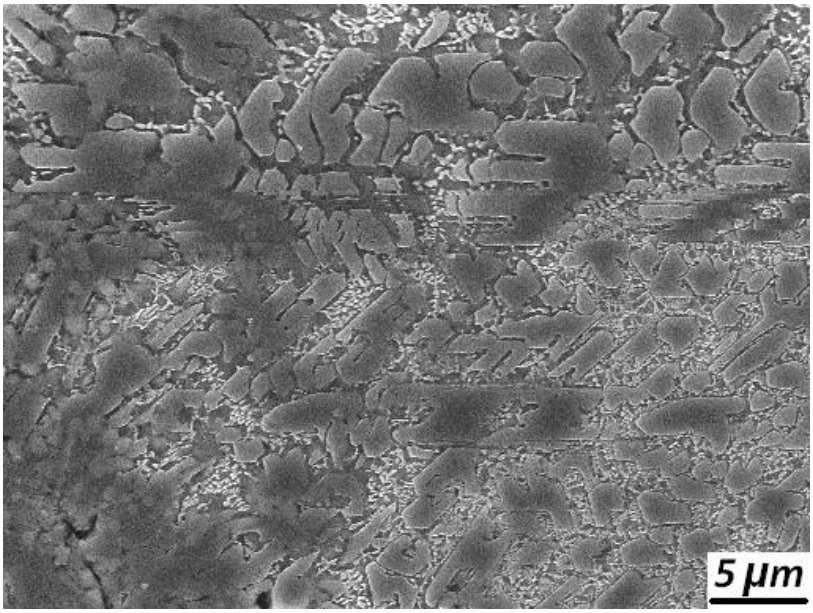

Figure 3-11: SEM micrograph of the dendrite arms in the sample S10

The DAS measurement results for three samples are reported in Table 3-3. The three samples have different scanning speeds and similar laser energy. It is noted that the DAS decreases significantly with increasing the laser scanning speed. Table 3-3 also includes

the corresponding cooling rate values for the different laser scanning speeds. The calculation of these values and their relation to the measured DAS will be discussed in Section 3.4.

Table 3-3: The calculated cooling rate for different scanning speed

Laser Scanning Speed (mm/s)	Cooling Rate (°C)	Average DAS (μm)
2 (S10)	$4.7x10^4$	2.9
3 (S9)	$7.0x10^4$	2.4
4 (S8)	$9.3x10^4$	2.0

3.3.3 Energy Dispersive Spectroscopy

EDS analysis provided further information on the composition of the dendrite arms and the porosity. The whole cross-sections were first tested to provide a general view of the percentage of Ni to Ti elements in the formed sample, as well as to determine if any unwanted materials were present. Figure 3-12 confirms the absence of any impurities in the cross-section of sample S8 as well as the presence of only nickel and titanium in the formed SMA. However, in some other tests, a small amount of iron (Fe) was found. The amount of Fe in these samples was strongly related to both scanning speed and energy input. That is, by increasing the energy input to the melt-pool and reducing the scanning speed, the amount of Fe increases. This makes sense since these conclusions lead to high energy input, which leads to more steel substrate melting and dilution of deposited layer with Fe.

Table 3-4 presents EDS results for three samples prepared using three different laser scanning speeds with all other parameters held constant. The EDS results for the porosity area in Figure 3-9 confirms that the area contains approximately a 2:1 atomic ratio of titanium and nickel, respectively, indicating that the solidified area has Ti_2Ni intermetallic phase. The dendrite arms were also tested and the results indicate that they contain a 3 to 4 atomic ratio of titanium and nickel, respectively. The only intermetallic phase with this ratio is Ti_3Ni_4. Further EDS analysis has provided information on the compositional variation of the sample cross sections. It is noted in Figure 3-13 that the

details of the composition profiles may vary when the measurements are made at different locations across the height of the deposited layer. The amount of Fe in the deposited layers decreased with moving away from the substrate until it totally disappeared as indicated in Figure 3-13.

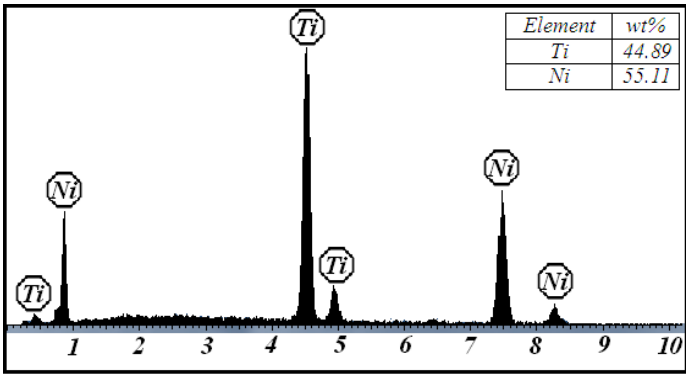

Figure 3-12: EDS result obtained for produced sample

Table 3-4: The EDS analysis of the bulk on average composition of deposited layers with different scanning speeds

Spectrum	Ti wt%	Ni wt%	Fe wt%
Low scanning speed (S15)	43.20	55.07	1.73
Medium scanning speed (S13)	44.18	54.69	1.13
High scanning speed (S11)	44.79	55.21	0

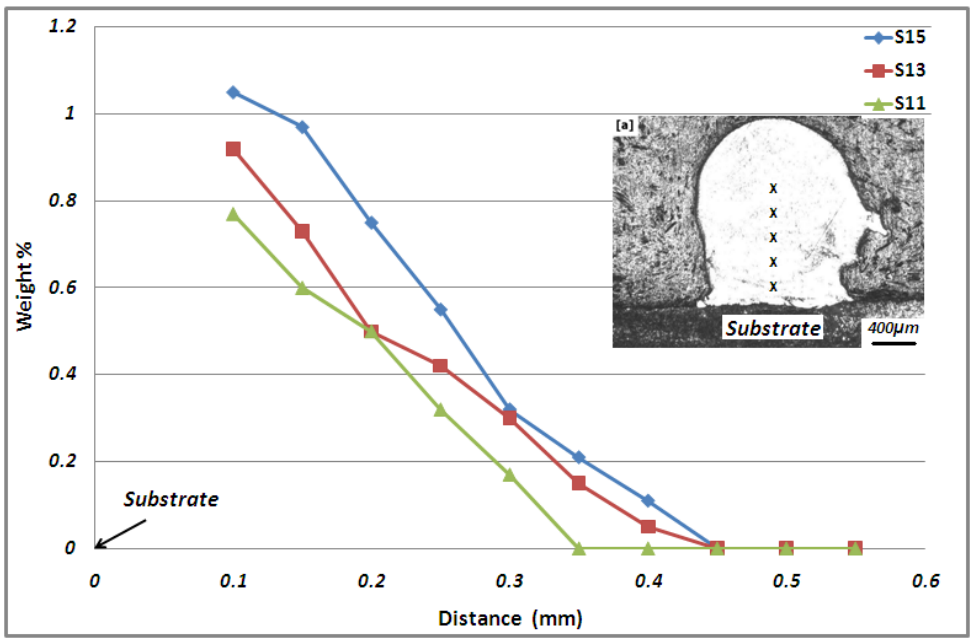

Figure 3-13: EDS results obtained for deposited samples processed with different input energies

3.3.4 X-Ray Diffraction

Multiple XRD experiments have been conducted on the prepared samples with different process parameters. The results of the first test conducted, on sample S13, are provided in Figure 3-14 (a). There was the intermetallic phase NiTi austenite (B2) and solid solution phase Kamacite (αFe, Ni). The presence of iron in the fabricated sample can be explained as a result of the high energy input applied to the melt-pool heating the substrate enough to melt and diffuse it to the deposited layer. On the other hand, the high scanning speed and low energy input used to produce sample S3 created a cross-section with only NiTi (B2), as seen in Figure 3-14 (c). In the case of sample S8, the phases found were NiTi martensite (B19') and Ti_2Ni, as shown in Figure 3-14 (b).

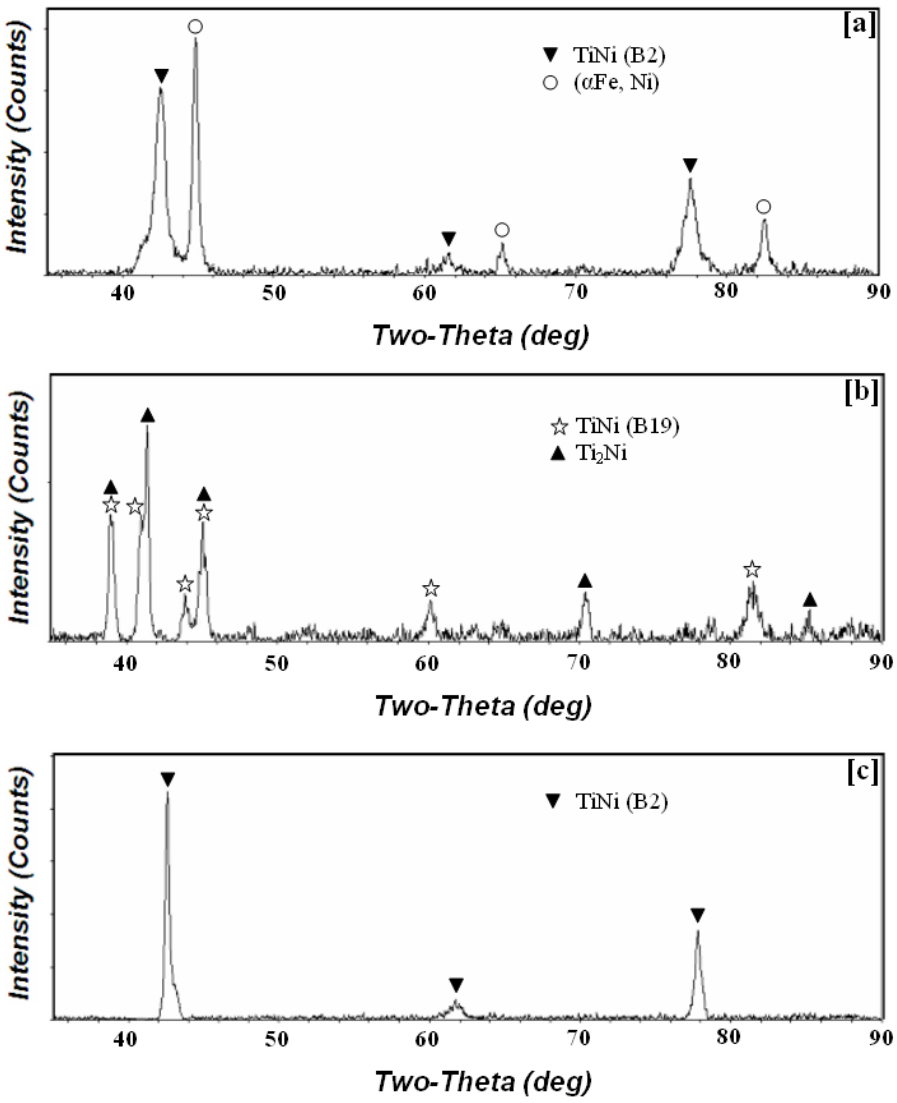

Figure 3-14: Exemplar XRD spectra of the sample cross-sections for samples processed with three different process parameters. (a) Sample S13, (b) Sample S8, and (c) Sample S3

3.3.5 Differential Scanning Calorimetry

Figure 3-15 presents the DSC results of SMA (Ni-Ti) wires manufactured using LSFF with several laser process parameters. Two samples from each range (high, medium and law input laser energy) were tested. Sample S8 was the only sample that showed martensitic behavior in the range of 25-120 ˚C, as indicated using DSC. By fixing the process parameters of sample S8 and adjusting the laser scanning speed, another sample

showed martensitic behavior in the same range (25-120 ˚C). The transformation temperatures had one stage in heating (B19')→(B2) and also one stage in cooling (B2)→(B19').

From the DSC curves, the transformation start and finish temperatures were determined by the intersection of a base line and the tangent to a peak. The martensitic transformation start temperature, M_s, varied from 60 to 65 ˚C in samples prepared using medium laser energy, such as sample S8, see Figure 3-15 (a). However, by increasing the laser scanning speed by a small value and fixing the other parameters of sample S8, M_s of sample S7 was varied from 37 to 42 ˚C, see Figure 3-15 (b). The curvaceous wires were also tested, see Figure 3-16. The results for sample C5 are very similar to those for sample S8.

The absorbed/released heat during the transformation process was calculated from the area under the curve of the heat flow between the start and finish temperatures of transformation from the thermogrammes obtained by differential scanning calorimetry. The difference between the areas was used to estimate the total energy dissipation in a full thermal cycle. Table 3-6 shows the amount of heat absorbed and released in the two straight samples tested (S7 and S8). A value of less than 2 J/g is much lower than the approximately 25 J/g expected from the Ni Ti transformation. Therefore, only a portion of the sample is NiTi (B19) which is consistent the XRD result of Figure 3-14.

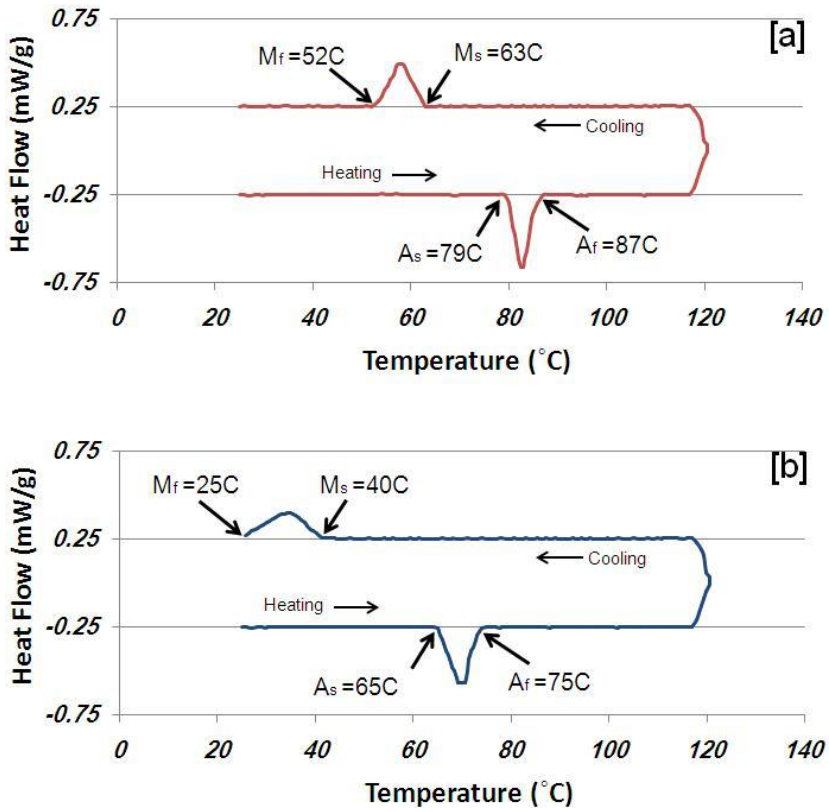

Figure 3-15: DSC curves for straight wires samples (a) S8 and (b) S7

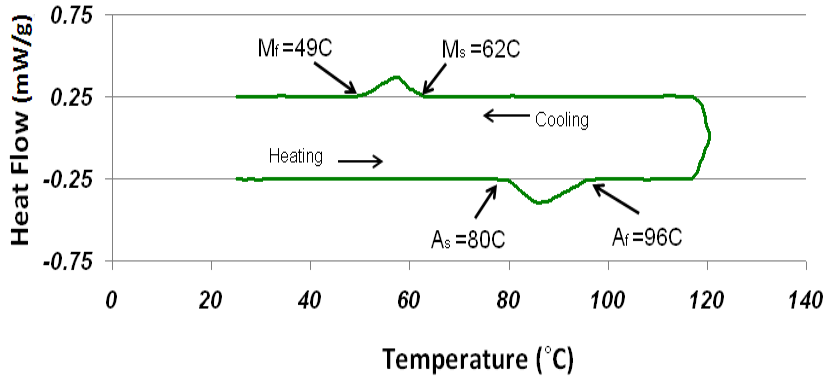

Figure 3-16: : DSC curves for curvaceous wire sample C5

Table 3-5: Absorbed/released heat

Sample #	Absorbed Heat (J/g)	Released Heat (J/g)
S7	1.875	1.6
S8	1.3125	1.375

3.3.6 Hardness

Microhardness results are presented in Figure 3-17. The hardness was measured in-situ using three different spots, at approximately the center of each wire's cross-section. Pre-placed powder thickness played a big role in the hardness of the fabricated wires. By increasing powder thickness, the porosity level is also increased reducing the hardness. The laser scanning speed also affects the hardness. The faster the scanning speed the harder the sample became. The hardness increased from 330 to 420 HV when the scanning speed was rosin from 2 to 5 mm/s.

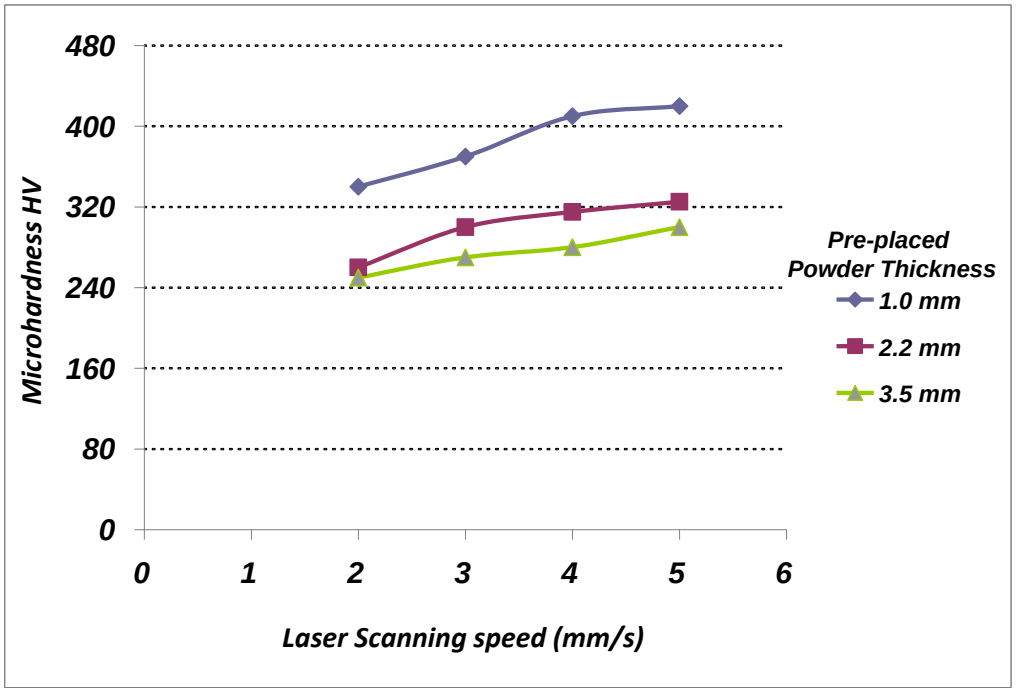

Figure 3-17: Hardness profile for prepared samples with different powder thickness

3.4 Discussion

Hard layers of Ni-Ti were successfully produced on thin mild steel plates using the pre-placed powder LSFF method. The combination of microscopy, XRD and hardness measurements indicates that a relative dense layer product can be produced. However, optimum layer conductions to produce, dense, homogeneous NiTi (B19) requires future research. The elimination of porosity by decreasing the initial powder thickness and the observation of porosity on a sample processed with the highest laser scanning speed, suggest that the porosity problem should be tackled by optimizing a combination of processing parameters. Complete elimination of the problem, particularly during handling and use of formed products, will also require further investigation into the correlated effects from thermal expansion anisotropy of Ti_2Ni [61].

Laser irradiation causes melting of the powder mixture. The dendritic microstructure of the coating is then formed and evolved during solidification of the melt-pool and subsequent cooling to room temperature [62]. The solidification rate is a function of the cooling rate in the melt-pool, which is in turn a function of the laser scanning speed. The relationship between the cooling rate ($\partial T/\partial t$) and the laser scanning speed is given by [63][64]:

$$\frac{\partial T}{\partial t} = -2\pi K \times \left(\frac{v}{P_t A} \right) \times \left(T_m - T_0 \right)^2 \qquad (3\text{-}1)$$

where K is the powder's thermal conductivity, v is the laser scanning speed, T_m is the melting temperature of the powder, T_0 is the ambient temperature, and A is the absorption factor.

The values of the above constant parameters in the present work are $K= 47.2$ (W/m.K), $T_m= 1310$ ºC , $T_0= 25$ ºC, and $A= 0.45$. The parameter P_t is the average laser power and is given by $P_t = EF$, where E is the laser pulse energy (i.e. 4 J per pulse) and F is the laser pulse frequency (i.e. 50 Hz). The cooling rate values for the current laser scanning speeds have been calculated using Equation (3-1) and the results have been listed in

Table 3-3. Comparing the results with the corresponding DAS values, it is clear that the higher cooling rates, which are achieved as a result of faster laser scanning speeds, result in finer microstructures (i.e. smaller DAS).

The EDS result provided in results section shows that the dendrite arms have approximately 3:4 atomic ratio of titanium and nickel, respectively, indicating that solidification begins with the dendritic formation of Ti_3Ni_4 phase. This phase is a metastable phase that should transfer to Ni-Ti if there is enough energy in the melt-pool. However, this situation can be resolved by heat treatment [65].

The EDS result for the porosity area in Figure 3-9 confirms that the area has an approximate 2:1 atomic ratio of titanium and nickel, respectively, indicating that the solidified area contains Ti_2Ni intermetallic phase. Similar solidification results for the same phase have also been reported by Man et al [61]. The XRD results further confirm the formation of this intermetallic compound (Ti_2Ni) in the formed layer, as shown in Figure 3-14. From XRD and EDS results in the case of the sample processed with higher input energy (S11-S15), small amount of Fe was presented in the formed layer.

Higher scanning speeds can lead to finer dendritic structures. It is well established that DAS influences the mechanical properties of alloys and a finer dendritic structure usually results in higher hardness [66]. Although the faster laser scanning speeds result in higher hardness levels, a lower scanning rate seems to be a better choice to eliminate the possibility of porosity and increase control of the process in order to melt the pre-placed powder completely. However, lower laser scanning speeds may also lead to oxide formation in the coating layer when no shield gas is used during processing.

3.5 Assessment of the SME of Fabricated SMA parts

The elasticity and the shape memory effect (SME) of the SMA parts was investigated first by bending the wires then heating them. Samples S8 and C5 (in Table 3-1 and 3-2) were the only samples used to conduct this test. By bending the wires above their elastic ranges and heating them above the transformation temperature, the maximum

deformation can be reached where the transformation temperatures were also determined. Three methods were used to heat the deformed wires in order to test the capability of regaining their shapes. These methods were: hot surface, hot water, and passing current.

As the name suggests, in the hot surface method wires were placed on a hot surface (i.e. 90 ºC) until they fully recovered their shapes, and recovery time was measured. Second method was carried out by dipping the deformed wires in hot water (i.e. 80 ºC). The recovery time in the hot water test was very fast; it did not exceed two seconds. The last method was performed by applying an electrical current to heat the wires. The power given to the deformed wires was calculated by first measuring the electrical resistance using an EMS Power Supply and then multiplying it by the passing current.

Figure 3-18 depicts the process used to measure the transformation temperature of (30×1×1) mm SMA straight wire using the hot surface method. The wire was bent to about 29˚ (maximum it could reach), as shown in Figure 3-18(a), before it was left on a hot surface (90 ˚C). After 2 seconds, the wire started to regain its original shape, the angle reduced to 20˚ (Figure 3-18(b)). One second later, the sample continued recovering and the angle became 19˚. The wire then needed two more seconds to reach its original shape (Figure 3-18(d)). Five seconds is the total time this wire needed to fully regain its shape with the selected testing procedure.

In the case of curvaceous wire, the hot surface test was also carried out. The 0.8 mm wire was deformed, as shown in Figure 3-19(a), prior to heating. Then, it was left to recover on a hot surface (90 ˚C). The whole process took about 7 seconds to reach the final shape in Figure 3-19(b).

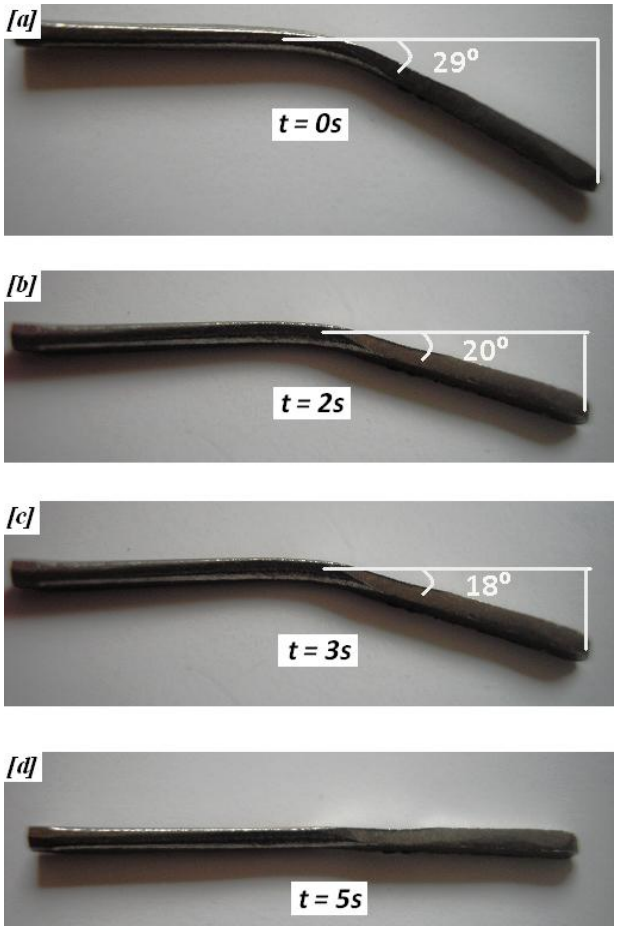

Figure 3-18: Fabricated straight SMA wire heated using hot surface

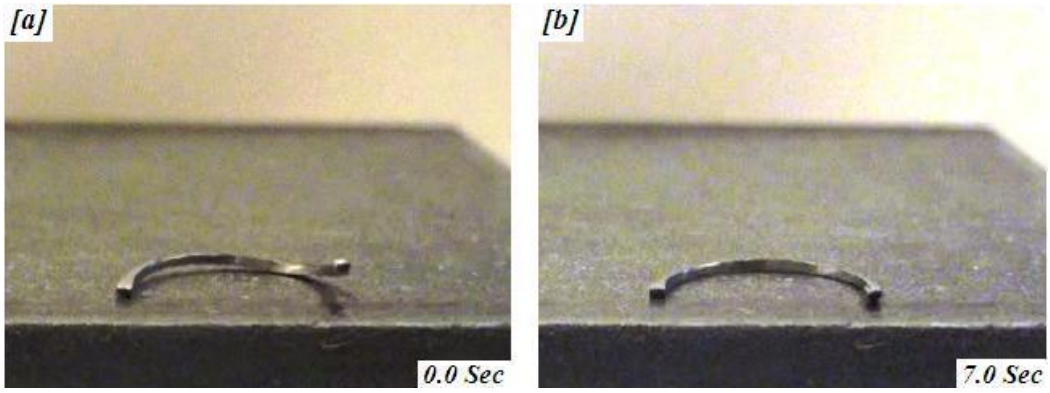

Figure 3-19: Fabricated curvaceous SMA wire heated using hot surface

The recovery test was also conducted by dipping the bent wire in hot water (80 ˚C). First, the wire was bent to about 29˚ and then was dipped in the hot water. With this type of heating, the wire took only two seconds to recover, see Figure 3-20.

Figure 3-20: Fabricated SMA straight wire heated using hot water

The passing current method was also used to heat bent SMA wires. First, the wire's geometries were measured using a digital caliper with 0.01 mm accuracy. The measured geometries were the semi-circular radius and the cross-section dimensions, as shown in Figure 3-21. The radius was fixed at 10 mm; however, the square cross-section dimension was varied from 1.2 mm in length and width to 0.6 mm.

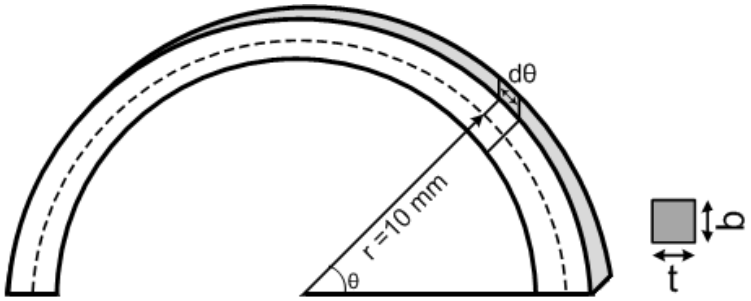

Figure 3-21: Schematic diagram of the semi-circular dimensions of SMA wire

The heating process was initiated by measuring the resistance of each wire. The cross-sectional dimensions and the electrical resistance relation is presented in Figure 3-21. Then, two values of current were applied to the wire: 1.8 A and 2.5 A. The wires were each connected to the power supply using small clips, as shown in Figure 3-22. Table 3-6 lists the time each wire needed to fully recover and regain their original shapes. Higher electrical resistance causes faster recovery. Figure 3-23 presents the relationship between the wire resistance and recovery time. Unsurprisingly, wire thickness also played a

significant role in recovery time. For example, while a 0.6 mm wire needed only one second with 2.5 A to regain its shape and 2.5 seconds with 1.8 A, a 1.2 mm wire needed 8 seconds with 1.8 A and 5 seconds with 2.5 A. This relation is graphically drawing in Figure 3-24. More tests were conducted using variety of currents in order to compare them with the numerical results later in Chapter 4.

Using different heating methods provides an idea of the recovery time the fabricated wires were required. The SME results from these tests prove the ability of the fabricated parts to recover very fast.

Figure 3-22: Curvaceous wire connected to the power supply

Table 3-6: Experimental results of a passing current heating test

t = b (mm)	I (A)	R (Ω)	Recovery time (sec) (Experiment)
1.2	2.5	0.085	5
1.2	1.8	0.085	8
1.0	2.5	0.11	3.5
1.0	1.8	0.11	5
0.8	2.5	0.13	1.5
0.8	1.8	0.13	3
0.6	2.5	0.2	1
0.6	1.8	0.2	2.5

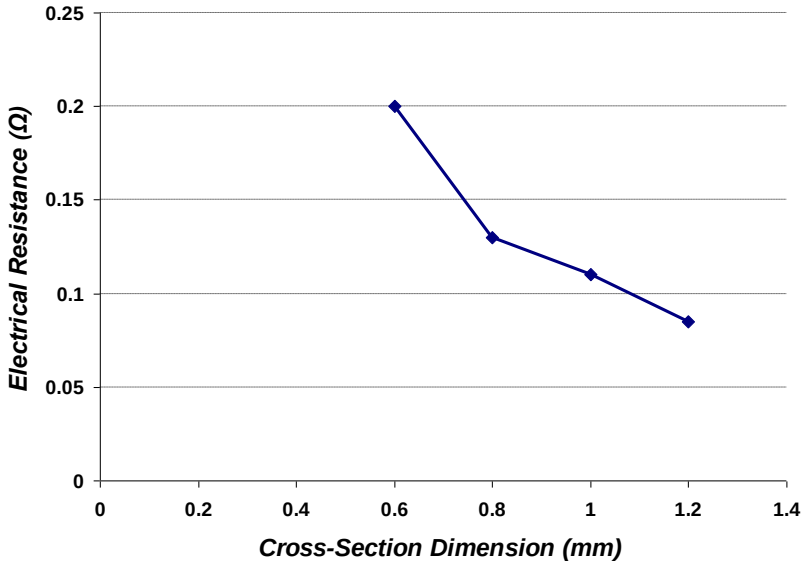

Figure 3-23: Dimension-electrical resistance relation for semi-circular wires

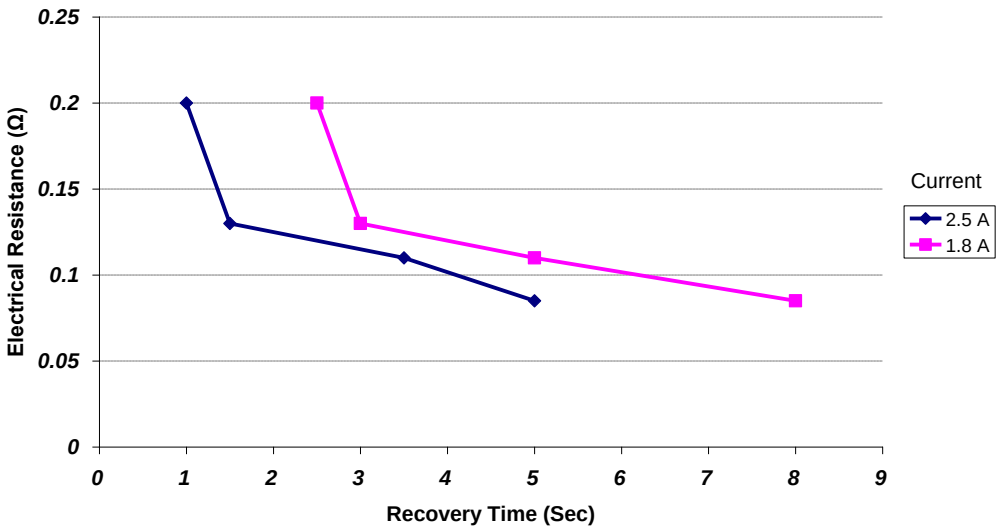

Figure 3-24: Recovery time for different wire sizes using two currents

3.6 Conclusions

In this study, SMA (Ni-Ti) wires were fabricated by Nd:YAG pre-placed LSFF. It was used to melt the Ni-Ti powder in a controlled shield gas atmosphere. Two shapes were fabricated: straight wires (30×1×1 mm) and curvaceous wires (Diameter = 20 mm) . The following conclusions can be drawn from fabricating Ni-Ti wires using different processing parameters:

1- Higher laser scanning speeds result in finer microstructure and higher hardness.

2- XRD results provide evidence for the formation of unwanted intermetallic such as αFe,Ni when a very low laser scanning speed was used.

3- A lack of energy input in the melt-pool creates wires with NiTi (B2) phase.

4- DSC results proved that higher scanning speeds cause shifting of the transformation temperature by about 20 ˚C.

5- Some of the fabricated samples (S7, S8 and C5) showed some SME even prior to any heat treatments for improving SME.

Chapter 4

Modeling of Shape Memory Alloy with Semi-Circular Shape

This chapter addresses the modeling of a semi-circular SMA wire using lump and finite element approaches. This model, which couples heat and stress-strain equations gains insight into the mechanical performance of the proposed geometry.

4.1 Heating Model

A one-dimensional heat transfer equation was proposed for a wire by Ikuta [59]. The heat transfer equation used in this study describes the wire's heat energy which is equal to the energy generated from electric resistance heating minus the energy lost due to convection. The wire's specific heat $\boldsymbol{c}$, volume V [m^3], surface area A [m^2], and density ρ [Kg/m^3] are assumed to be independent of temperature. The temperature of the surroundings is T_0 [ºC]. Assuming Q [W] is the electrical input power and h_0 [$W/(m^2\ ºC)$] is the convection heat transfer coefficient, the energy equation is presented by:

$$\rho c V \frac{\partial T}{\partial t} + h_0 A(T - T_0) = Q \tag{4-1}$$

In the above energy equation, the temperature is assumed to be unique throughout the whole wire, which only varies with the time, not the location, in the wire. This is a valid assumption as the wire is small in size. The heat transfer by radiation in the temperature range of 25-60 ºC is very small compared to the heat transfer by convection [68]. As a result, radiation is ignored in Equation (4-1).

Input electrical energy and temperature are found to be functions of time. The electrical energy can be calculated as $Q = Ri^2$ where R is resistance [Ω] and i is the current [A]. Since the change in the wire's resistance is less than 10% with any temperature changes, it is assumed to be constant in this study. The thermal expansion is ignored due to the wires small sizes.

The mass of each wire was measured using an analytical balance (Sartorius YDK01, The Sartorius Group) accurate to ±0.001 g. The volume was measured using a volume-based approach with accuracy of ±0.1 ml. Having both observation parameters, the density of the fabricated wires was calculated.

4.2 Stress-Strain Relationship

As discussed in previous chapters, a SMA wire in general has three crystalline phases: austenite, R-phase, and martensite. However, the R-phase will not be considered in the modeling because of its negligible effect on SMA properties.

One of the properties that changes during phase transformation in SMAs is the yield strength. The austenite phase has only one lattice structure and it is in the elastic region (Figure 4-1(a)). Martensitic behavior, on the other hand, can be better understood by examining a typical stress-strain curve for the martensite phase (Figure 4-1(b)). The material acts elastically when a small stress is applied, as represented in Figure 4-2(b) (which corresponds to region 0 to 1 in Figure 4-1(b)). As stress is increased the material yields (region 1) and de-twinning occurs (between regions 1 and 2). Eventually, the martensitic structure becomes entirely de-twinned, as represented by Figure 4-2(c) (which corresponds to region 2 Figure 4-1(b)), at which point a second elastic region

occurs (between regions 2 and 3). If stress continues to be applied permanent plastic deformation begins (region 3), after which the original shape is not recoverable by the SME.

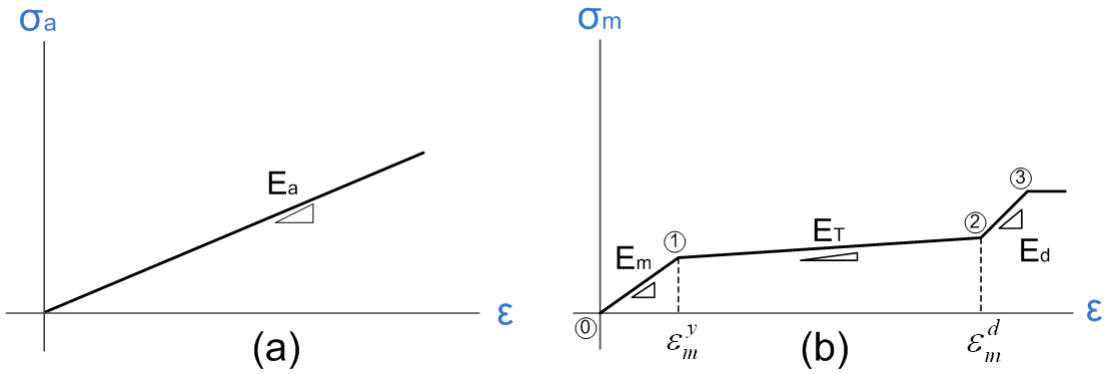

Figure 4-1: Stress-Strain curve for (a) Austenite SMA. (b)Twinned Martensite SMA

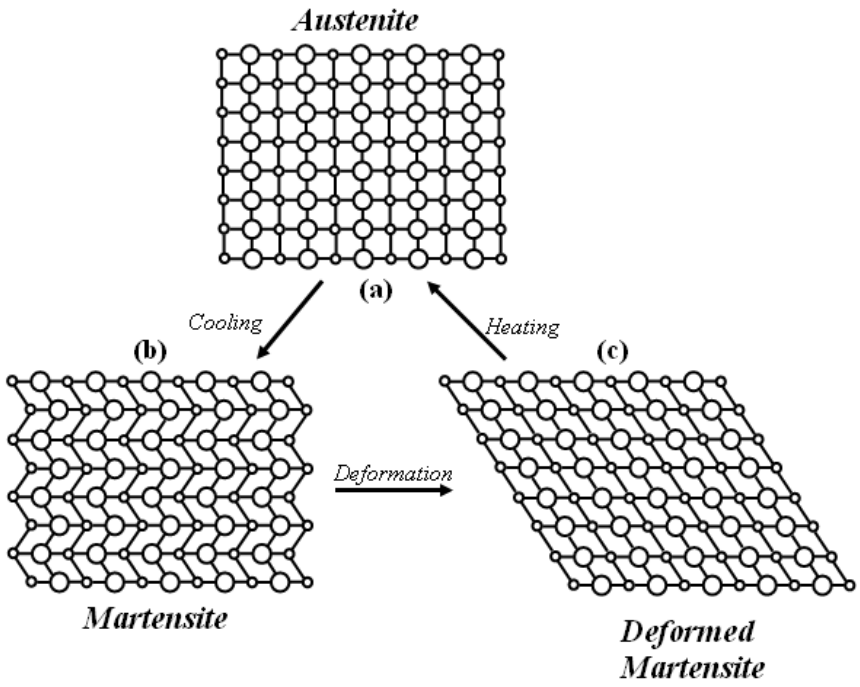

Figure 4-2: Material crystalline arrangement during the Shape Memory Effect

Each phase (austenite and martensite) gives additively to the total stress in the material. At a particular value of strain ε, assume that σ is the associated stress, and σ_a is the resulting stress in the part if it were completely austenite. Also, assume σ_m is the resulting

stress in the part if it were completely martensite. If R_a and R_m are the respective phase fractions of austenite and martensite in the beam then the total stress equation is:

$$\sigma(\varepsilon) = R_a \sigma_a(\varepsilon) + R_m \sigma_m(\varepsilon) \tag{4-2}$$

Since the R-phase is ignored, the additive effect of the austenite and martensite ratios equals to one *(R_a + R_m = 1)*. Then, the total stress equation in terms of R_m, that is substituted with ξ will be:

$$\sigma(\varepsilon) = (1-\xi)\sigma_a(\varepsilon) + \xi\sigma_m(\varepsilon) \tag{4-3}$$

If the material is completely austenite at high temperature, it acts elastically until it yields, and the stress-strain relationship can be presented as:

$$\sigma_a(\varepsilon) = E_a \varepsilon \tag{4-4}$$

where E_a is the young elastic modulus of the austenite phase.

Because there are three phases in fully martensitic material, the martensite stress-strain relationship becomes:

$$\sigma_m(\varepsilon) = \begin{cases} E_m \varepsilon \ldots\ldots\ldots\

$$\sigma(\varepsilon)=\begin{cases} E_m\varepsilon\xi+(1-\xi)E_a\varepsilon \ldots\ldots\ldots\ldots\ldots\ldots\ldots\ldots\ldots\ldots\ldots\ldots 0\le\varepsilon<\varepsilon_m^y \\ E_m\varepsilon_m^y\xi+E_T\xi(\varepsilon-\varepsilon_m^y)+(1-\xi)E_a\varepsilon \ldots\ldots\ldots\ldots\ldots\ldots\ldots\ldots\ldots \varepsilon_m^y\le\varepsilon<\varepsilon_m^d \\ E_m\varepsilon_m^y\xi+E_T\xi(\varepsilon_m^d-\varepsilon_m^y)+E_d\xi(\varepsilon-\varepsilon_m^d)+(1-\xi)E_a\varepsilon \ldots\ldots\ldots \varepsilon_m^d<\varepsilon \end{cases} \quad (4\text{-}6)$$

The above equation can also be expressed to solve ε as shown in Equation (4-7)

$$\varepsilon=\begin{cases} \dfrac{\sigma}{E_a-(E_a-E_m)\xi} \ldots\ldots\ldots\ldots\ldots\ldots\ldots\ldots\ldots\ldots 0\le\varepsilon<\varepsilon_m^y \\ \dfrac{\sigma+\xi(E_T-E_m)\varepsilon_m^y}{E_a-(E_a-E_T)\xi} \ldots\ldots\ldots\ldots\ldots\ldots\ldots\ldots\ldots\ldots \varepsilon_m^y<\varepsilon\le\varepsilon_m^d \\ \dfrac{\sigma+\xi(E_T-E_m)\varepsilon_m^y+(E_d-E_T)\varepsilon_m^d}{E_a-(E_a-E_d)\xi} \ldots\ldots\ldots\ldots \varepsilon_m^y<\varepsilon \end{cases} \quad (4\text{-}7)$$

4.3 Martensite Fraction Model

The martensite fraction model links the temperature equation and the stress-strain relation. The martensite-fraction temperature relationship by Ikuta can be presented as: [69]

$$\xi(T)=\frac{\xi_a}{[1+e^{K(T-T_m-C_m\sigma)}]}+\xi_b \quad (4\text{-}8)$$

where K is a temperature constant, C_m is the reciprocal of the stress rate, and T_m is the average transformation temperature.

Constants ξ_a and ξ_b were selected by Ikuta to be 1 and 0, and they represent a gain and an offset, respectively. However, the other constants, T_m and K, depend on whether the material is in a heating or cooling stage. For cooling:

$$T_m=\frac{T_s^M+T_f^M}{2} \text{ and } K=\frac{6.20}{T_s^M-T_f^M} \quad (4\text{-}9)$$

and for heating:

$$T_m = \frac{T_s^A + T_f^A}{2} \text{ and } K = \frac{6.20}{T_f^A - T_s^A} \tag{4-10}$$

where the constant 6.20 was determined empirically [59]. T_s^A, T_f^A, T_s^M, and T_f^M are defined as the start and finish temperatures of austenite and martensite, respectively.

The above equations can only generate the major loop of the martensite-fraction temperature relationship. To include the minor loops, ξ_a and ξ_b should not be kept constant. The superscripts C and H are used to identify whether the material is in cooling or in heating stage, respectively.

Given the ambient temperature T_0, Assume $\Delta T = T - T_0$, and K^C and K^H are two positive "temperature" constants that can be determined from the slope of the T-to-ξ curve [69]. Constants β^C and β^H are defined in Equations (4-11) and (4-12), respectively, as:

$$\beta^C = \frac{T_s^M + T_f^M}{2} - T_0 + C_m\sigma \tag{4-11}$$

$$\beta^H = \frac{T_s^A + T_f^A}{2} - T_0 + C_m\sigma \tag{4-12}$$

Now, the new martensite-fraction temperature relation will be presented in two equations, the first for cooling and the second for heating stages. To incorporate the minor loops, the relation should be written in terms of time and temperature. Equation (4-8) can be split into the two following equations for cooling and heating, respectively. [69]

$$\xi^C(\Delta T;t) = \frac{\xi_a^C(t)}{[1+e^{k^C(\Delta T-\beta^C)}]} + \xi_b^C(t) \tag{4-13}$$

$$\xi^H(\Delta T;t) = \frac{\xi_a^H(t)}{[1+e^{k^H(\Delta T-\beta^H)}]} + \xi_b^H(t) \tag{4-14}$$

The functions ξ_a^C, ξ_b^C, ξ_a^H, and ξ_b^H remain constant as long as the material is being heated or cooled (no switching between them). Only when these functions change from H-to-C or from C-to-H should $\xi(\Delta T,t)$ be kept continuous.

At time t = 0, ξ_a^C, ξ_b^C, ξ_a^H, and ξ_b^H have initial conditions which have been given as:

$$\xi_a^C(0) = \xi_{a0}[1 + e^{-K^C\beta^C}] \text{ and } \xi_b^C(0) = \xi_{b0} \tag{4-15}$$

$$\xi_a^H(0) = \xi_{a0}[1 + e^{-K^H\beta^H}] \text{ and } \xi_b^H(0) = \xi_{b0} \tag{4-16}$$

where ξ_{a0} and ξ_{a0} are constants listed in Table 4-1.

While a SMA material is heating, $\xi(\Delta T,t) = \xi^H(\Delta T,t)$ as shown by Equation (4-16), and when it is cooling, $\xi(\Delta T,t) = \xi^C(\Delta T,t)$ as shown by Equation (4-15). To sustain continuity while the process changes from cooling to heating or vice-versa, there must be switching conditions at switching time (t_S) at switching temperature (T_S). The corresponding equations for these switching conditions are listed below. [69]

Switching Condition: Heating to Cooling:

$$\xi_a^C(t_S) = [\xi_{a0} + \xi_{b0} - \xi^H(T_S;t_S)]\frac{(1+e^{-k^C\beta^C})(1+e^{-k^C(T_S-\beta^C)})}{e^{k^C(T_S-\beta^C)} - e^{-k^C\beta^C}} \tag{4-17}$$

$$\xi_b^C(t_S) = \xi_{a0} + \xi_{b0} - \frac{\xi^C(T_S;t_S)}{1+e^{-k^C\beta^C}} \tag{4-18}$$

Switching Condition: Cooling to Heating:

$$\xi_a^H(t_S) = [\xi^C(T_S;t_S) - \xi_{b0}](1+e^{k^H(T_S-\beta^H)}) \tag{4-19}$$

$$\xi_b^H(t_S) = \xi_{b0} \tag{4-20}$$

For simulation, the parameters listed in Table 4-1 were used.

Table 4-1: Simulation Parameters

Property	***Value***	***Unit***	***Reference***
Constant: initial (ξ_{a0})	1		[69]
Constant: initial (ξ_{b0})	0		[69]
Constant: Reciprocal of stress rate (C_m)	0.23	$\frac{°C}{MPa}$	,[69]
Constant: Temperature cooling (K^C)	0.053	$\frac{1}{°C}$	[69]
Constant: Temperature heating (K^H)	0.07	$\frac{1}{°C}$	[69]
Convection heat transfer coefficient (h_0)	75	$\frac{W}{m^2 °C}$	[69]
Density (ρ)	5200	$\frac{Kg}{m^3}$	Exp
Specific heat (C_P)	460	$\frac{1}{Kg°C}$	[69]
Strain – martensite detwin (ε_m^d)	0.0596	$\frac{m}{m}$	[69]
Strain – austenite twin (ε_m^y)	0.0136	$\frac{m}{m}$	[69]
Temperature ambient (°C)	25	°C	
Martensite finishes temperature (T^M_f)	52	°C	Exp (DSC)
Martensite starts temperature (T^M_s)	63	°C	Exp (DSC)
Austenite finishes temperature (T^A_f)	87	°C	Exp (DSC)
Austenite starts temperature (T^A_s)	79	°C	Exp (DSC)
Elastic of austenite (E_a)	35917	MPa	[69]
Elastic of fully twinned martensite (E_m)	16800	MPa	[69]
Elastic of partly twinned martensite (E_T)	826	MPa	[69]
Elastic of detwinned martensite (E_d)	16800	MPa	[69]

4.4 Geometrical Domain for the Simulation

To perform the numerical analysis, the geometrical domain shown in Figure 4-3 was proposed for this study. To calculate the total strain in a straight wire, the following equation is typically used:

$$\varepsilon = \frac{dl}{l} \tag{4-21}$$

However, some corrections must be made to this equation for it to be useful for modeling SMA wires with semi-circular shapes. Since $dl = rd\theta$ and $l = \pi r$, the total strain equation for the semi-circular shape can be written as:

$$\varepsilon = \frac{rd\theta}{\pi r} \tag{4-22}$$

The proposed radii of the wires was fixed at 10 mm; however the cross-sectional dimensions actually varied from 0.6 mm to 1.2 mm (see table Table 4-2).

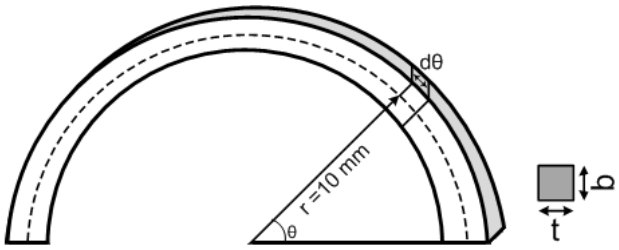

Figure 4-3: Proposed geometrical domain

Table 4-2: Wire's Cross-Section Dimensions

Sample	***t=*** ***mm***	***b=*** ***mm***
0.6 mm	*0.6*	*0.6*
0.8 mm	*0.8*	*0.8*
1.0 mm	*1.0*	*1.0*
1.2 mm	*1.2*	*1.2*

4.5 Simulation results

In this work, two types of model were considered. The first attempted to simulate a passing current heating method. And the second attempted to simulate a one end heating method. For the first model, only MATLAB® was used and for the second model, COMSOL® in addition to MATLAB® were used.

4.5.1 Passing Current Model

Solving this model began with applying the heating model in Equation (4-1). Figure 4-4 shows the current steps used as inputs in the heating model. The current was set to jump to 1.3 A every 60 seconds and remain steady for 10 seconds. The results from solving Equation (4-1) for a 0.6 mm wire is shown in Figure 4-5. The temperature increased to 130 ºC when the current was on. Then, the wire needed about 30 seconds to cool back down to ambient temperature.

In the case of 1.2 mm wire, a 1.3 A current was not enough to heat the wire above its transformation temperature. Consequently, a 3.0 A current was used to heat the 1.2 mm wire. The results from solving Equation (4-1) is shown in Figure 4-6. The 1.2 mm wire needed almost the entire 60 seconds between inputs to cool down to ambient temperature.

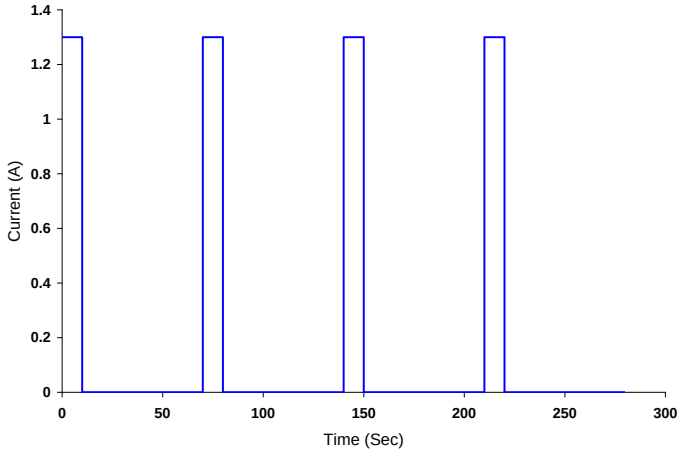

Figure 4-4: Current step used for 0.6 mm wire

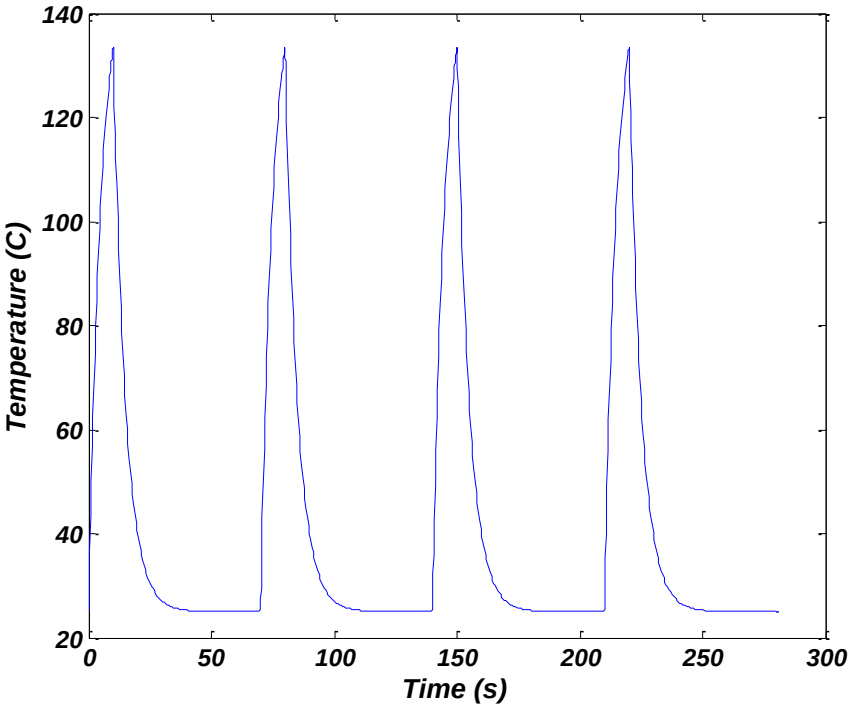

Figure 4-5: Temperature-Time relation for 0.6 mm wire using 1.3 A current

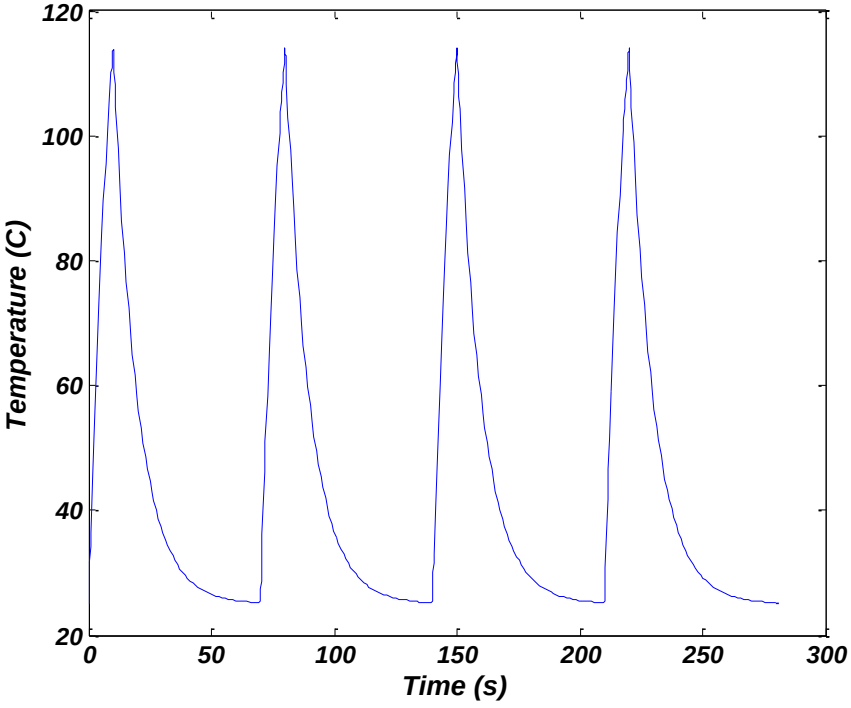

Figure 4-6: Temperature-Time relation for 1.2 mm wire using 3.0 A current

The martensite fraction model was also solved using MATLAB. Figure 4-7 shows the relationship that occurred between the martensite fraction (ξ) and temperature for a 0.6 mm wire. The material was in the martensite phase until heat was applied. Then, it started transforming into austenite as the temperature increased. When the wire was left to cool, the material returned to its original phase, martensite, using another slope.

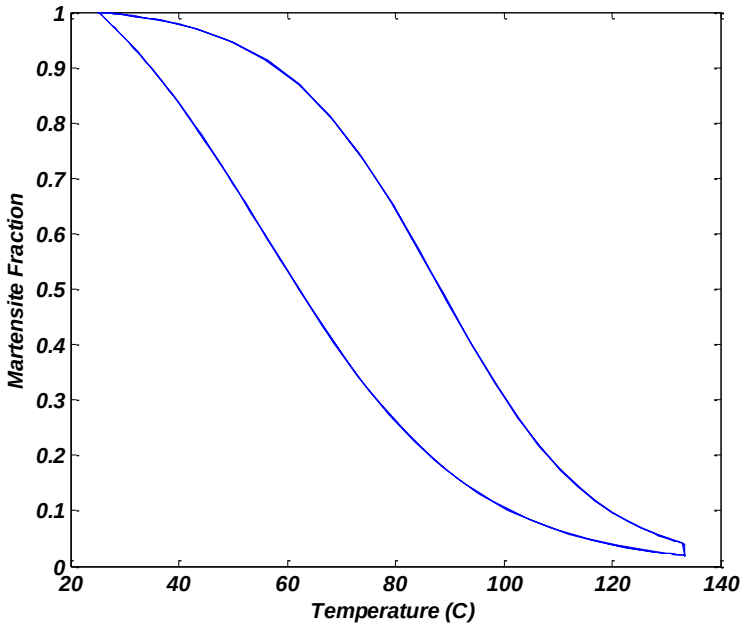

Figure 4-7: Martensite fraction-Temperature relationship for the 0.6 wire

The stress-strain model in Equation (4-7) was applied to measure the time needed for each wire to fully regain its shape. Figure 4-8 and 4-9 give an idea of how many seconds each wire needed to recover. A 0.6 mm wire (Figure 4-8) required approximately 5 seconds of continuous current at 1.3 A to fully recover. However, in the case of 1.2 mm wire (Figure 4-9) at least 10 seconds of continuous current at 3.0 A was required.

To measure the total strain, the stress-strain relation in Equation (4-8) was used. In this model, a fixed stress (σ = 277 MPa) was applied. The results from the MATLAB model for a passing current are shown in Figure 4-8 and Figure 4-9. A total strain–time relationship for the 0.6 mm wire shows that the wire needs about 5 seconds of heating with a 1.3 A current to change from martensite to austenite. In contrast, the same wire

requires approximately 45 seconds from the time the passing current is removed before it is fully converted to martensite again (see Figure 4-8).

On the other hand, the 1.2 mm wire follows the same path but at different rates. During heating, the wire needed about 10 seconds to change from martensite to austenite and almost 60 seconds to return to martensite when the heat was taken away.

The other two wires (0.8 and 1.0 mm) was also tested. The compared results are in Table 4-3.

Table 4-3: Comparison between transformation times for different samples

Sample	Current (A)	Resistance (Ω)	Mart → Aust Transformation Time (Sec)	Aust → Mart Transformation Time (Sec)
0.6 mm	1.3	0.2	5	45
0.8 mm	2.0	0.13	7	50
1.0 mm	2.8	0.11	8.5	55
1.2 mm	3.0	0.085	10	60

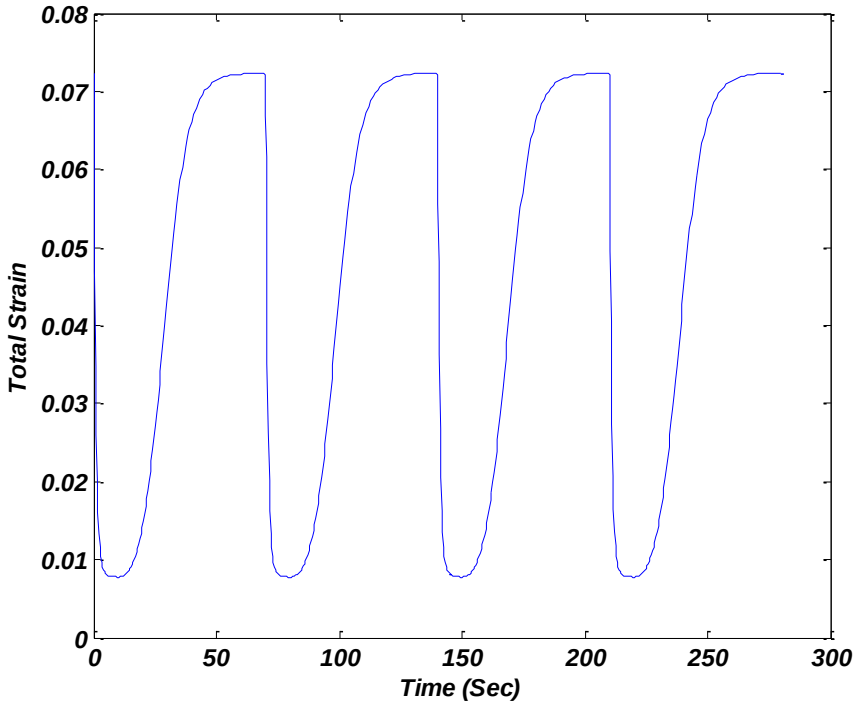

Figure 4-8: Total strain for 0.6 mm wire using passing current

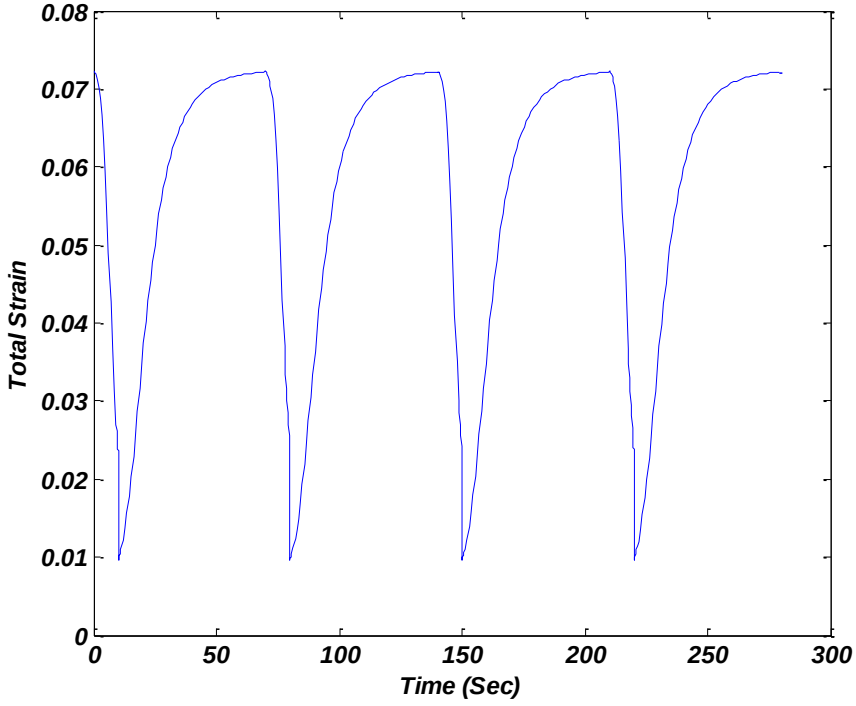

Figure 4-9: Total strain for 1.2 mm wire using passing current

4.5.2 One End Heating

Modeling a curvaceous wire by heating its one end and measuring the strain at the second end was conducted. Solving this model began with drawing the wires using SOLDWORKS® software. Then, the drawn parts were imported to COMSOL® to apply the boundary and sub-domain settings.

The boundary settings were set to 150 °C at one end of the wire and convective flux at the other surfaces. In the sub-domain setting, the parameters listed in Table 4-1 were used. In addition, convection heat transfer was also enabled.

Before solving this model, the parts were meshed. To reach mesh independency, several attempts were carried out. The models were solved for a different numbers of meshes, from small numbers to high. The minimum temperature from each solution was listed and compared with the rest. The number of meshes kept increasing until a steady state in the temperature was reached (see Figure 4-10). Mesh independence was reached when the number of meshes is more than 25,000 or the size of the element is less than 0.0005 mm. Figure 4-11 and Figure 4-12 show the meshed 0.6 mm and 1.2 mm wires, respectively.

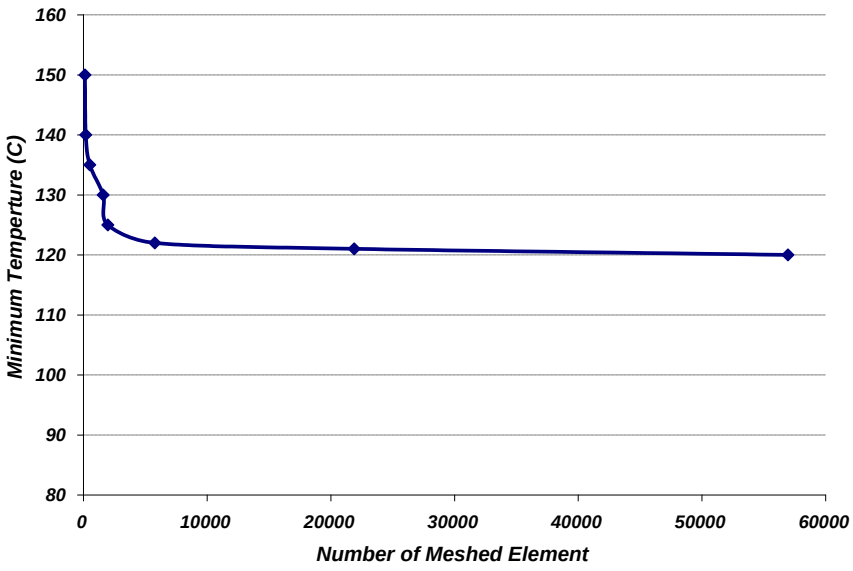

Figure 4-10: Mesh Independency Analysis

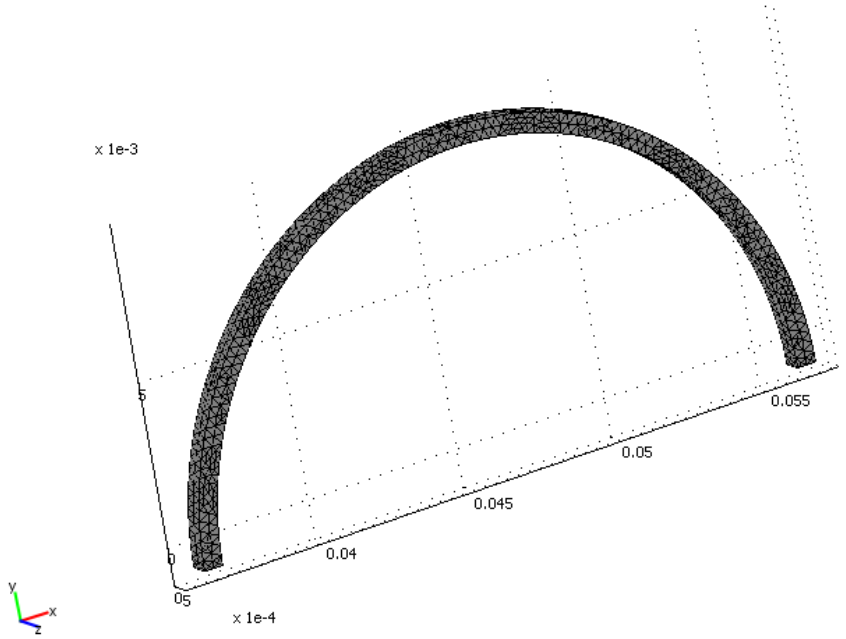

Figure 4-11: Meshed 0.6 mm wire

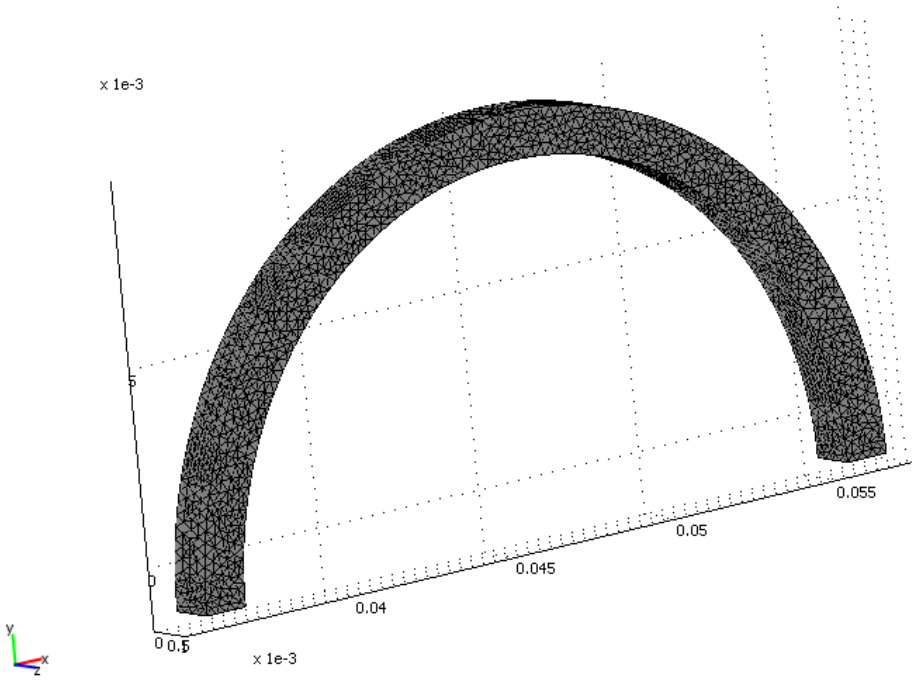

Figure 4-12: Meshed 1.2 mm wire

After reaching the a convenient number of elements, it was time to solve the model. A time dependant solver was used with solving time step of 0:0.1:10 seconds. Figure 4-13 illustrates the solved thermal model for the 0.6 mm wire. The result indicate that the minimum temperature in the unheated end is 103 °C. The temperature increases by moving toward the other end until it reaches the maximum temperature at 150 °C. When the same conditions were applied to solve the model for the1.2 mm wire (Figure 4-14), the results indicate that the minimum temperature rises to 125 °C. The increase in minimum temperature in the thicker samples might have resulted from the larger contact area between the wire and the hot surface.

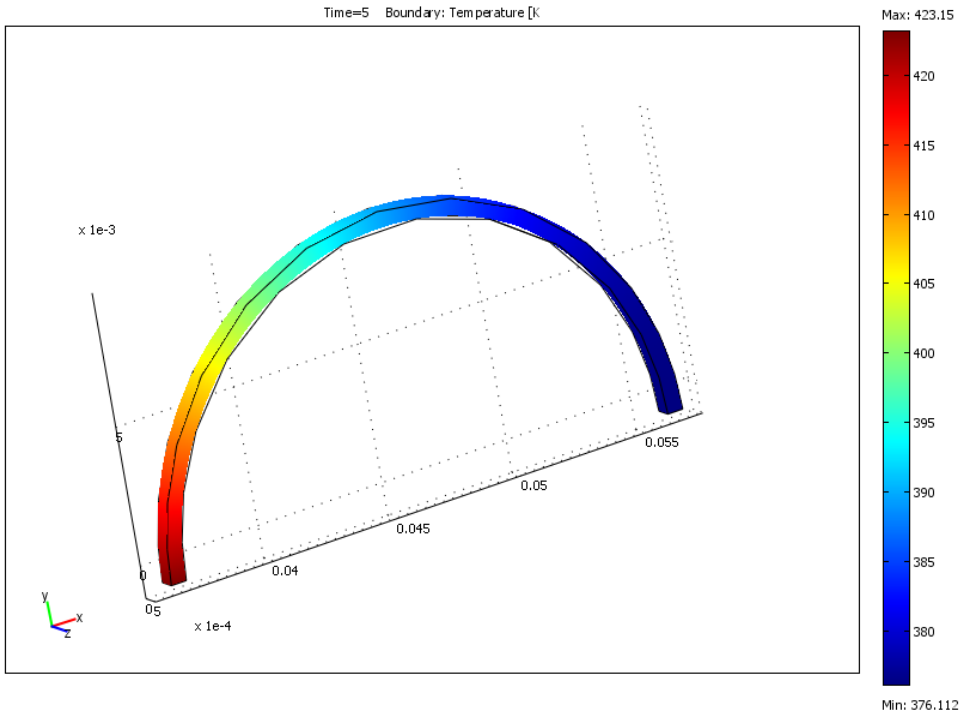

Figure 4-13: Solved model for 0.6 mm wire

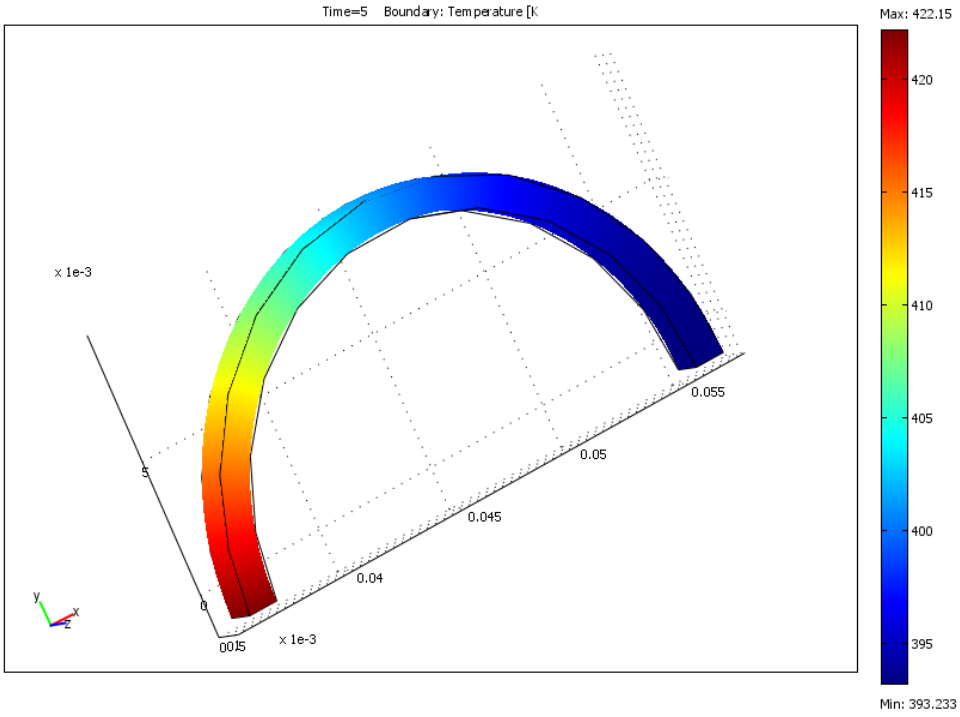

Figure 4-14: Solved model for 1.2 mm wire

The temperature-time gradient was then exported for the purpose of using it in the MATLAB model. The same steps in section 4.5.1were followed to solve the stress-strain equation. The wires in this model were set to cool down for 100 seconds. The results in Figure 4-15 and Figure 4-16 suggest that the unheated end of the 0.6 mm wire needed about 9.5 seconds to convert phases while the 1.2 mm wire required 10 seconds to reach the same result. In the cooling process, the 1.2 mm wire took 75 seconds to cool off; however, the 0.6 mm wire took only 35 seconds.

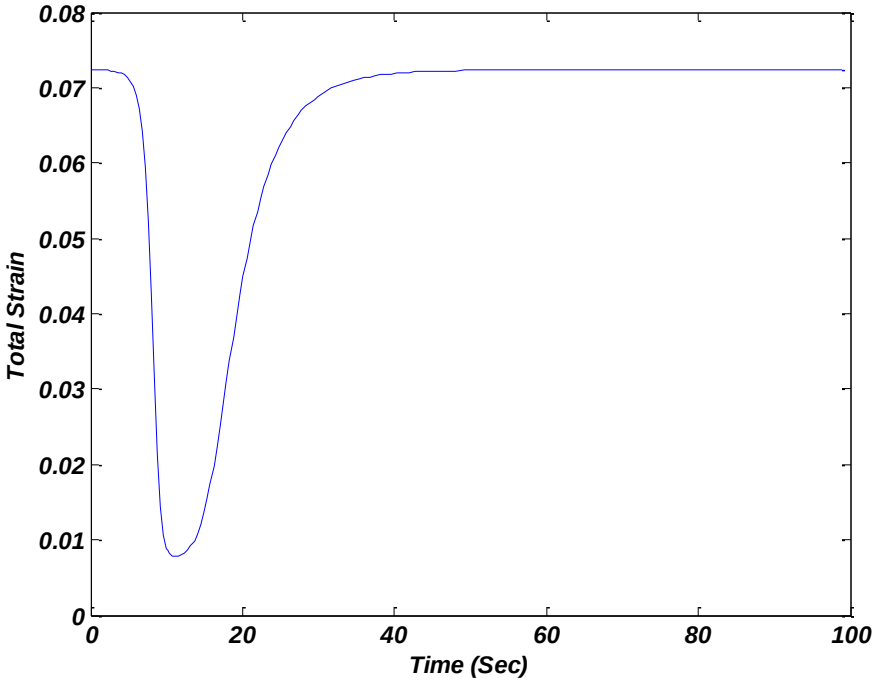

Figure 4-15: Total strain for 0.6 mm wire using one end heating

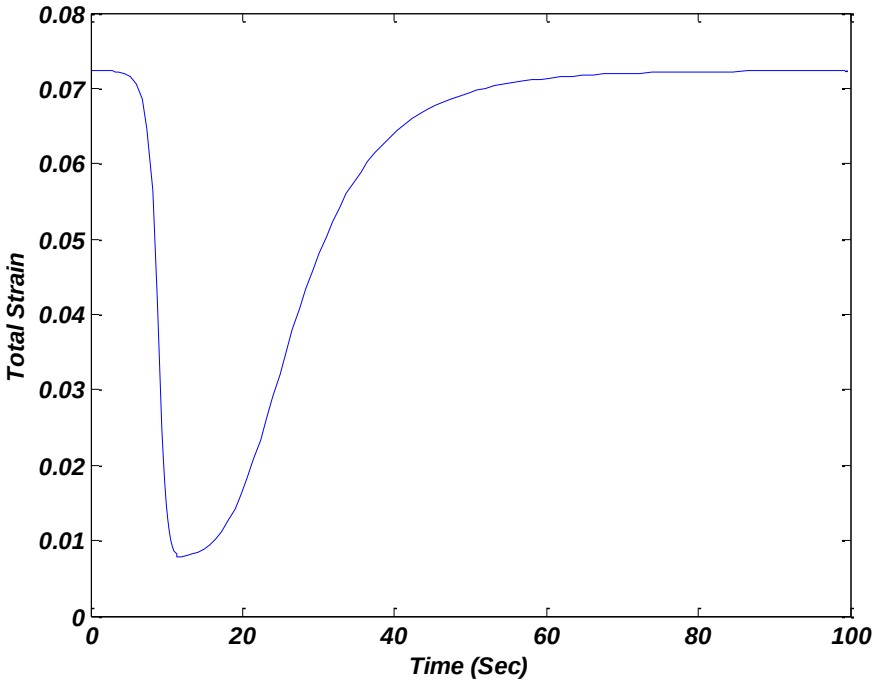

Figure 4-16: Total strain for 1.2 mm wire using one end heating

4.6 Comparison of Numerical and Experimental Results

To compare the SME numerical and experimental results, results from both tests were graphed in Figure 4-17. The results from the passing current tests indicate that there is good agreement between the numerical and experimental tests. Indeed, the differences in the recovery times between the tests is less than 0.5 seconds in most of the samples.

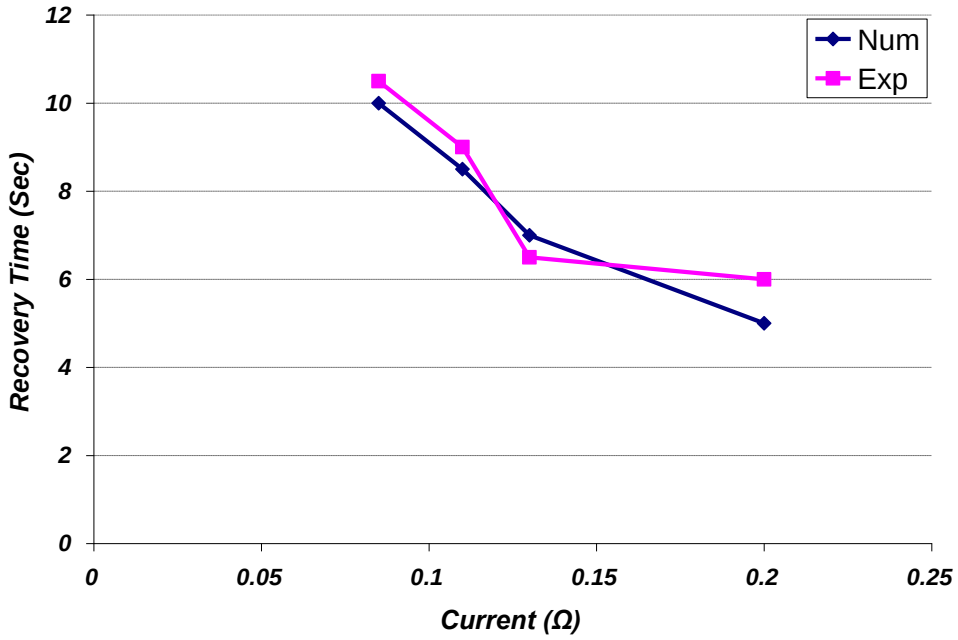

Figure 4-17: Numerical - Experimental results Comparison

4.7 Conclusions

The following conclusions can be drawn based on the studies conducted in this chapter:

1. The findings of this study prove the relation between wires size and recovery time.
2. The passing current model using MATLAB showed that the larger the electrical resistance of a wire, the faster it recovered. For example, the 0.6 mm wire with 0.2 Ω needed half the time the 1.2 mm wire with 0.085 Ω needed.

3. The results from the one end heating model using MATLAB and COMSOL showed the weak relation this model led to between the wire size and the recovery time. All the wires needed almost the same period of time to recover.
4. The compared results between the numerical and experimental approaches proved a good match relation exists between the tests.

Chapter 5

Conclusions and Future Work

This thesis presented an assessment of pre-placed LSFF for manufacturing a shape memory alloy (Ni-Ti) with complex geometries. A mixture of 55.2 wt%Ni - 44.8 wt%Ti powder was used to produce different sizes and shapes of SMA wires. In LSFF, some of the processing parameters such as scanning speed and laser energy were varied to investigate the effect of each parameter on the samples properties. The following conclusions can be drawn based on the studies conducted in this work:

1- Increasing the scanning speed produces harder samples than what is produced at low speeds; however, higher scanning speeds reduces the energy available in the melt-pool, producing samples with porosity.

2- The scanning speed may also affect transformation temperatures; for example, increasing scanning speed by only 1 mm/s led to production of samples with significantly higher transformation temperatures (by up to 10ºC).

3- The thickness of the pre-placed powder played a significant role in some of the sample properties, such as hardness. By reducing the powder thickness by half, the hardness of the cross section could increase by HV80.

4- The XRD results for different samples show that different intermetallics occur with different laser energy. For example, with very low scanning speed, unwanted intermetallic can be formed (i.e., αFe,Ni).

5- The lump theoretical model presented a clear relation between sample size and recovery time. That is, reducing the sample size from 1.2 mm to 0.6 mm results in a significant reduction in the recovery time (i.e., from 10 to 5 s).
6- In the second FE approach (one end heating), the sample size – recovery time relation was not as good as the first model. The results indicated that only a 0.5 s difference between the 1.2 mm and 0.6 mm wires in the recovery time.
7- Comparison of the numerical-experimental results suggested good agreement between the two tests.

In the future, the following studies can be conducted:

1. Other SMA powder materials (e.g., Copper-Aluminium-Nickel) may be tested using the same method.
2. Instead of pre-placed LSFF, the powder injection method can be considered to melt the powder.
3. The mechanical characteristics of the fabricated samples can be investigated more thoroughly using fatigue tests.
4. The finite element model can be improved for more accurate results by solving the stress-strain equation.
5. The process parameters can be examined more through changing the fixed parameters in this study such as frequency and pulse width.

References

[1] Miyazaki, S.: Development and Characterization of Shape Memory Alloys. In: Fremond, M.; and Miyazaki, S.: Shape Memory Alloy, 1996 by CISM.

[2] Funakubo, H. Shape Memory Alloy, (1987). Gordon and Breach Science Publisher.

[3] Detailed Introduction to Shape Memory Alloys. http://smart.tamu.edu/overview/overview.html

[4] Institute of Mechanics and Computational Mechanics. http://www.ibnm.unihannover.de/Forschung/Projekte/sagar.pt/index.html.en

[5] Wikipedia, the free encyclopedia, Shape memory alloys. http://en.wikipedia.org/wiki/Shape_memory_alloy.

[6] Youyi, E.; Hsu, T.Y.; and Ko, T.: Shape Memory Alloy. 1986 China Academic Publishers.

[7] Fan, G.; Zhou, Y.; Otsuka, K.; Ren, X.; Nakamura, K.; Ohba, T.; Suzki, T.; Yoshida, I.; and Yin, F.: Effects of Frequency, Composition, Hydrogen and Twin Boundary Density on the Internal Friction on Ti50Ni50-xCux Shape Memory Alloy. Acta Materialia (2006) 54, n 19, 5221-5229.

[8] Niu, L.P.; Sakuma, T.; Takaku, H.; Kyogoku, H.; and Sakai, Y.: Erosion Resistance of Ti-Ni Shape Memory Alloy to Hot Water Jet. Material science Forum (2002) 394-395, 353-356.

[9] Bahia, M.G.; Gonzalez, B.M.; and Buono, V.T.L.: Fatigue Behaviour of Nickel-Titanium Superelastic Wires and Endodontic Instruments. Fatigue Fracture Engineering Structure (2006) 29, 518-523.

[10] Rigo, O.D.; Otudo, J.; Moura Neto, C.; and Mei, P.R.: NiTi SMA Production Using Ceramic Filter during Pouring the Melt. Journal of materials processing Technology (2005) 162-163, 116-120.

[11] Chang, S.H.; Wu, S.K.; and Chang G.H.: Transformation sequence in Several Cold-Rolled and Annealed $Ti_{50}Ni_{50}$ Alloy. Materials Science and Engineering A (2006) 438-440, 509-512.

[12] Liang, C., The Constitutive Modeling of Shape Memory Alloys. Ph.D. thesis Virginia Tech. (1990)

[13] Harrison, J.D. and Hodgson, D.E.: Shape Memory Effect in Alloys, Plenum (1975).

[14] Miwa, Y., Iguchi, N., Honma, D., and Nishimura, T.: Proceeding of the Japan Society of Precision Engineering, Nagoya (1982).

[15] Mulder, B.J.: Vacuum, 26, p. 31 (1976).

[16] Advanced Dental Concepts. http://andoverdmd.com/treatment_dentures.html

[17] Sachdeva, R. and Miyazaki, S.: Proceeding MRS International Mtg on Advanced Materials., 9, p. 445 (1989).

[18] Ryhänen, J.: Biocompatibility evolution of nickel-titanium shape memory alloy. Academic Dissertation, Finland (1999).

[19] LINK, Medical Device, The Online Information Source of the medical Device Indestry (2003). http://www.devicelink.com/

[20] NMT Medical, Inc. (2001). http://www.nmtmedical.com.

[21] Duerig, T.M., Pelton A. and Stöckel, D.: An overview of NITINOL medical applications. Materials Science and Engineering A, 273-275: 149-160 (1999)..

[22] Raychem (2001). http://www.raychem.com

[23] Mantovani D. Shape memory alloys: Properties and biomedical applications. Journal of the Minerals, Metals and Materials Society, 52: 36-44 (2000).

[24] SMA/MEMS Research Group (2001). http://database.cs.ualberta.ca/MEMS/sma_mems.

[25] Cook Medical, (2002). http://www.cookmedical.com.

[26] ASTM Standard Specification F2063-00 (American Society for Testing and Materials, 2000).

[27] Bunshah, R.F; Techniques of Metals Research, Vol. 1. part 2. (Interscience Publishers 1968)

[28] Suzuki, Y; Fabrication of Shape memory alloys (Shape memory Materials, ed; Otsuka, K. and Wayman, C.M.) 1998.

[29] Suzuki, Y. Proceeding MRS International Mtg on Advanced Materials., 9, p. 557. (1989).

[30] Thomas Net Institute newsroom. http://news.thomasnet.com/index.html

[31] Muller, K.; Proceedings, 8th International Conference on Metal Forming, Krakow, Poland, p. 657 (2000).

[32] Yoshida, K.J. the Japan Society for Technology of Plasticity, Vol.31, No.355), p.1015 (1990.

[33] Wu, S.K.; Lin, H.C.; and Yen, Y.C.: Materials Science & Engineering A, Vol.215, No.1-2, p.113 (1996).

[34] Matsuo, A.; Ito, Y, and Gotou, N.: NiTi Based Alloy Wire And Its Production, Japanese Patent Publication JP08117835A (1996).

[35] Matsuo, A.; Ito Y. and Gotou, N.: Method For Thinning Wire Of NiTi Series Alloy, Japanese Patent Publication JP08112614A (1996).

[36] DiCello, J.A.; Minhas, B.S.; Simpson, J.W.; Cornelius, R.S. and Harrison, J.D.: Process for The Manufacture of Metal Tubes, United State Patent 5,709,021 (1998).

[37] Machine Center Inc. Precision machined parts for industry (2004) www.machinecenter.com.

[38] Suzuki, Y. Applications of Shape memory alloy (Funakubo, H. Shape Memory Alloy, (1987). Gordon and Breach Science Publisher).

[39] Miyazaki, S.; Kimura, S.; Takei, F.; Miura, T. Otsuka, K. and Suzuki, Y.; Scripta Metall., Vol.17, p.1057 (1983).

[40] Lee, J.H; Lee, H.W.; Ahn, J.G.; Chung, H.K. and Song, K.: Proceedings, International Conference on Shape Memory and Superelasticity Technologies, Antwerp, Belgium, p.33 (1999).

[41] Maiman, T.H.: “Stimulated optical radiation in ruby,” in Nature. 1960.

[42] Steen, W.M.; and Courtney, C.G.H.: “Surface heat treatment of En8 steel using a 2kW continuous-wave CO2 laser,” Metals Technology, vol. 6, no. 12, pp. 456—462, 1979.

[43] Steen, W.M.; and Courtney, C.G.H.: “Hardfacing of nimonic 75 using 2kW continuous-wave CO2 laser,” Metals Technology, vol. 7, no. 6, pp. 232-237, 1980.

[44] Toyserkani, E.; Khajepour, A.; and Corbin S.: "Laser Cladding" CRC Press. 2004.

[45] Abe, F.; Osakada, K.; Shiomi, M.; Uematsu, K.; and Matsumoto, M.: The manufacturing of hard tools from metallic powders by selective laser melting. Journal of Materials Processing Technology (2001) 111, 210-213.

[46] Das, S.: Physical aspects of process control in selective laser sintering of metals. Advanced Engineering Materials (2003) 5, no. 10, 701—711.

[47] Tang, Y.; Loh, H.T.; Wong, Y.S.; Fuh, J.Y.H.; Lu, L.; and Wang, X.: Direct laser sintering of a copper-based alloy for creating three-dimensional metal parts. Journal of Materials Processing Technology (2003) 140, no. 1-3, 368—372.

[48] Powell, J.; Henry, P.S. and Steen W.M., “Laser cladding with preplaced powder: Analysis of thermal cycling and dilution,” Surface Engineering, vol. 4, no. 2, pp. 141—149, 1988.

[49] Malukhin, K. and Ehmann, K. Material Characterization of NiTi Based Memory Alloys Fabricated by the Laser Direct Metal Deposition Process. Journal of Manufacturing Science and Engineering. Vol. 128 p. 691 (2006)

[50] Robert, G.; Damjanovic, D. and Setter, N.: Preisach modeling of piezoelectric nonlineariry in ferroelectric ceramics. Journal of Applied Physics, 89, 5067-5074, 2001.

[51] Tanaka, K.; A thermomechanical sketch of shape memory effect: one-dimensional tensile behaviour. Res Mech, 18, pp. 251-263, 1986.

[52] Tanaka, K.; Kobayashi, S. and Sato, Y.: Thermomechanics of transformation, pseudoelasticity and shape memory effect in alloys. Int. J. Plast, 2, pp. 59-72.

[53] Liang, C. and Rogers, C. A.: One-dimensional thermomechanical constitutive relations for shape memory materials. Journal of Intelligent Material Systems and Structures, 1, pp. 207-234, 1990.

[54] Brinson, L. C.; One-dimentional constitutive behavior of shape memory alloys: thermomechanical derivation with non-constant material functions and redefined martensite internal variable. Journal of Intelligent Material Systems and Structures, 4, pp. 229-242, 1993.

[55] Boyd, J. G. and Lagoudas, D. C. Thermomechanical response of shape memory composites. Journal of Intelligent Material Systems and Structures, 5, pp. 333-346, 1994.

[56] Ivshin, Y. and Pence, T. J.: A constitutive model for hysterestic phase transition behavior. Int J Eng Sci.,32, pp. 681-704, 1994.

[57] Ivshin, Y. and Pence, T. J.: A thermomechanical model for a one variant shape memory material. Journal of Intelligent Material Systems and Structures, 5, pp. 455-473.

[58] Shaw, J. A.: A thermomechanical model for a 1-D shape memory alloy wire with propagating instabilities. Int. J. Solids Struct., 39, pp. 1275-1305, 2002.

[59] Ikuta, K.: Micro/miniature shape memory alloy actuator, in Proc. Int. Conf. Robot. Automat, p. 2156–2161 (1990).

[60] Murry, J. L.: Bulletin of Alloy Phase Diagrams, 3 (1992) 74-85.

[61] Man, H.C.; Zhang, S.; Cheng, F.T.; and Guo, X.: Laser Fabrication of Porous Surface Layer on NiTi Shape Memory Alloy. Materials Science and Engineering A 404 (2005) 173-178.

[62] Flemings, M.C.: Solidification Processing, McGraw-Hill, NY, USA, 1974.

[63] Audebert, F.; Colaco, R.; Vilar, R. and Sirkin, H.: Scripta Materialia 48(3) (2003) 281.

[64] Yue, T. M.; Huang, K. J. and Man. H. C.: Journal of Materials Science 39 (2004) 6599 – 6602.

[65] Frenzea, J.; Zhang, Z.; Somsen, Ch.; Neuking, K.; and Eggeler, G.: Influence of Carbon on Martensitic Phase Transformations in NiTi Shape Memory Alloys. Acta Materialia, (2007) 55, 1331-1341.

[66] Jansson, A.; Ion, J. C. and Kujanpaa, V.: Proceedings of SPIE, v: 4831 (2003), p: 475.

[67] Hutmacher, D.W., Sittinger, M., Risbud, M.V., (2004), "Scaffold-based tissue engineering: rationale for computer-aided design and solid free-form fabrication systems", *TRENDS in Biotechnology*, Vol. 22 No. 7, pp. 354-362.

[68] Incropera, F. and DeWitt, D.: Fundamentals of Heat and Mass Transfer. New York, New York: John Wiley & Sons, 4th ed., 1996.

[69] Madill, D. R.: "Modelling and stability of a shape memory alloy position control system," Master's of Applied Science, University of Waterloo, Waterloo, Ontario, 1993.

[70] Johnson Matthey, Inc., "Nitinol technical data\application notes." [Online]. Available: http://www.jmmedical.com/html/resource library.html, July 2004.

Appendicess

Appendix A

The MATLAB code written to solve the total strain for the fabricated samples.

1. The Heat Equation Code:

```
global rho c R L d V A T0 hu Cu
rho = 5200;
c=  460;
R = 0.2;

d=19.7/1000;
D=20.3/1000;
th=D-d;
V=pi/8*(D^2-d^2)*th;

A=2*pi/8*(D^2-d^2)+pi*th/4*(D+d)+2*th^2;
hu = 70;
T0=25;
options = odeset('RelTol',1e-5,'AbsTol',1e-5);
[t T]=ode45(@(t,T)Temperature(t,T),[0,200],T0,options);
plot (t,T);
xlabel('Time (s)');
ylabel('Temperature (C)');
```

2. The Martensit Fraction Code

```
global Mf Ms As Af Kmc Kmh Cm Rma0 Rmb0 Bc Bh
global rho c R L d V A T0 hu
Mf = 49;
Ms = 63;
As = 80;
Af = 96;

Kmc = 0.053;
Kmh = 0.07;
Cm = 0.23;
Rma0 = 1;
Rmb0 = 0;
sigma=277;

emy=0.0136;
Ea=35917;
Em=16800;
Et= 826;

Bc=0.5*(Ms+Mf)-T0+Cm*sigma;
```

```
Bh=0.5*(As+Af)-T0+Cm*sigma;
Rmac=Rma0*(1+exp(-Kmc*Bc));
Rmah=Rma0*(1+exp(-Kmh*Bh));

RmR_M=[];
t_M=[];
T_M=[];
sw=1;
Rma=Rmah;
Rmb=Rmb0;

for i=1:length (T)-1
    fi=sw;
if T(i)<T(i+1)
    B=Bh;
    Km=Kmh;
    Rma=Rmah;
    sw=1;
else
    B=Bc;
    Km=Kmc;
    Rma=Rmac;
    sw=0;
end
if sw>fi
    Rma=(RmR-Rmb0)*(1+exp(Kmh*(T(i)-T0-Bh)));
    Rmb=Rmb0;

elseif fi<sw
    Rma=(Rma0+Rmb0-RmR)*(((1+exp(-Kmc*Bc))*(1+exp(Kmc*(T(i)-T0-
Bc))))/(exp(Kmc*(T(i)-T0-Bc))-exp(-Kmc*Bc)));
    Rmb=Rma0+Rmb0-((Rma)/(1+exp(-Kmc*Bc)));
else
    sigma=277;
end

ex=exp(Km*((T(i)-T0)-B));
RmR=Rma/(1+ex)+Rmb;
RmR_M=[RmR_M RmR];

t_M=[t_M t(i)];
T_M=[T_M T(i)];
end
```

3. The Total Strain Code

```
global rho c R L d V A T0 hu
global Mf Ms As Af Kmc Kmh Cm Rma0 Rmb0 Bc Bh

ep=0;
ep_M=[];
for j=1: length (T_M)
if (ep(j)>0) & (ep(j)<emy);
ep(j)=sigma/(Ea-(Ea-Em)*RmR_M);
elseif (ep(j)>emy) & (ep(j)<emd)
ep(j)=(sigma+RmR_M*(Et-Em)*emy)/(Ea-(Ea-Et)*RmR_M);
else
ep(j)=(sigma+ RmR_M*(Et-Em)*emy+(Ed-Et)*emd)/ (Ea-(Ea-Ed)*RmR_M);
end
ep=[ep_M ep(j)];
end
```

4. The COMSOL to MATLAB Code

```
M=[]
for i=1:50
a=postinterp(fem,'T',[0.0362;-5.243e-4;0.0004],'solnum',i)
M=[M;a]
end
```